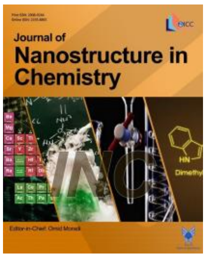

J. Nanostruct Chem. 2026; 16(5): 443-463

Journal of Nanostructure in Chemistry (JNSC)

https://doi.org/10.57647/jnsc.2026.1605.23

Research Article

A Hygrothermal Plate Theory with Intrinsic Transverse Normal Strain for Predicting Interlaminar Stresses Accurately in Functionally Graded Graphene Nanoplatelet Composite Plates

Rui Ma[1,2], Yuan Hu[3], Hongliang Li[4], Fanzeng Guo[5], Mingran Zhang[1], Abdul Ghaffar[1], Sadam Hussain[1], Manyu Zhang[1,*], Qilin Jin[6,*]

[1] *College of Mechanical Engineering, Quzhou University, Quzhou 324000, China*

[2] *Zhejiang Key Laboratory of Intelligent Manufacturing for Aerodynamic Equipment, College of Mechanical Engineering, Quzhou University, Quzhou 324000, Zhejiang, China*

[3] *Department of Aerospace and Mechanical Engineering, South East Technological University, Carlow, Ireland*

[4] *Zhongzhe High-Speed Railway Bearing Co., Ltd. No. 33 Yongtai Road, Longyou Economic Development Zone, Quzhou 324400, China*

[5] *Department of Aeronautics, Imperial College London, South Kensington Campus, City and Guilds Building, Exhibition Road, SW7 2AZ, London, UK*

[6] *School of Engineering, Hangzhou City University, Hangzhou 310015, China*

[*] **Corresponding authors:** zmy19940916@stu.xjtu.edu.cn, jinqilin0404@163.com

Article History:

Received:
03 February 2026

Revised:
03 April 2026

Accepted:
04 May 2026

Published in Issue:
31 October 2026

Abstract

Graphene based nanocomposites have great mechanical properties which could be applied in multifunctional engineering. But it is also true that classical higher order theory cannot provide a good description of the interlaminar mechanical behavior of FG-GNPRC laminate under moisture and thermal condition. It's a big difference because of the different parts in hygrothermal expansion coefficient causing dissimilar elasticity so there will be very complicated stress distribution. We have then developed another modified plate formulation with moisture and temperature induced strain taken up by the definition of displacement field, which means it is incorporated into the kinematic description so as not to add any further unknowns to our model. The proposed model can have an exact interlaminar shear stress because there are no breaks between layer and temperature-humidity. Also, the removal of the curvature-related terms of in- plane displacements from shear stress expression simplifies the finite element implementation. It's verified by comparison to 3D elasticity solutions and a few other classical theoretical models, which all show good agreement with the interlaminar stresses and deformations characterized here: And the parametric analysis shows more clearly what is governing the hygrothermal response. As we increase the GNP with some value and transverse deformations become large for having greater hygrothermal extension difference between low volumes but this is not true when increasing concentrations go on up to more amount. When we get quite different variation in GNP graduation across width that alters how stresses will behave from layer to layer, stress too by heat and water besides deformation and evolution of stress also depends on geometry proportion, stack configuration, applied load. All in all, they give structural response. These results can help in choosing suitable material gradation and structural design to improve the hygrothermal behavior of FG-GNPRC plates.

Keywords: Graphene nanoplatelets; Hygrothermal loading; Plate model; Transverse deformation

Cite this article: Ma R., Hu Y., Li H., Guo F., Zhang M, Ghaffar A., Hussain S., Zhang M., Jin Q.A Hygrothermal Plate Theory with Intrinsic Transverse Normal Strain for Predicting Interlaminar Stresses Accurately in Functionally Graded Graphene Nanoplatelet Composite Plates. *J Nanostruct Chem* **16**, 443-463 (2026). https://doi.org/10.57647/jnsc.2026.1605.23

1. Introduction

Graphene-based composite system has drawn much notice of the material science exploration at present for its excellent multi-function, consists of a good physical strength, good heat resistance and also good electric conductivity. The intensive quantitative characterization of thermal response characteristics of those newly developed advanced hybrid materials formulates as significant academic topic, particularly for high-risk engineering application scenes like aerospace thrust generation system, automotive heating arrangement and other cutting-edge miniaturized electronics. Current research foci have been on architectures of graphene nanoplatelets (GNPs), which exhibit improved structural stability and load-bearing performance in the nanocomposite matrix under varied working conditions [1,2]. In that regard, then, interdisciplinary research about the basic mechanical behavior in a GO augmented system has been activated here by a kind of such a technological paradigm [3-6] and new territory has emerged in the domain of composite science.

Current investigations indicate that there has been an explosive growth in the academic community focus on analyzing the mechanical performance attributes of FG-GNPRC frameworks [7-12]. Principal efforts in investigation have been placed on the creation of full analytical frameworks for the creation of the coupled thermomechanical response and constitutive relationship shown by the graphene reinforced heterogeneous matrix with non-uniform thermal and mechanical loads. Recent developments in the coupled thermal and mechanical evaluation of FG-GNPRC have been extensively documented through sophisticated analytical frameworks. Eyvazian et al. [13] examined thermo-mechanical instability in rotating FG-GNPRC microscale beams. Utilizing first-order theory (FSDT), Bidzard et al. [14] investigated thermal-vibration coupling effects within FG-GNPRC toroidal microstructures. Khorasani et al. [15] conducted size-dependent thermo-mechanical stability analysis in honeycomb plates with FG-GNPRC face sheets. By implementing a novel methodology, Sobhy [16] established a magneto-hygrothermal model for sandwich-curved nanocomposite panels. Mojiri and Salami [17] studied vibration behavior of FG-GNPRC beam on elastic bases with thermal effects. Furthermore, Eroğlu et al. [18] assessed the stability behavior of doubly curved sandwich shells featuring graphene-reinforced foam core. Zhang et al. [19] conducted the vibration analysis of piezoelectric FG-GNPRC plates possessing distributed porosity subjected to multifield loads. Nam et al. [20] analyzed the critical performance of shell-type sandwich panels made from FG-GNPRC. Employing nonlocal framework, Li et al. [21] performed an analysis of thermal-elastic bending wave dispersion in functionally graded microbeams enhanced with GNPs and CNTs. Bui et al. [22] evaluated time-dependent dynamic and bifurcation behaviors exhibited by FG-GNPRC shell and plate structures supported on viscoelastic substrates. Liu et al. [23] assessed the thermomechanical performance of porous FG-GNPRC plates. Li et al. [24] initiated a stability evaluation for submarine pipeline networks incorporating FG-GNPRC protective coatings. In microscale contexts, Li et al. [25] assessed thermal post-buckling characteristic of FG-GNPRC microtubes. Nam et al. [26] created parametric instability maps for FG-GNPRC toroidal shell structures with corrugated cores in the thermal environment. Songsuwan et al. [27] performed comparative stability analysis of perfect and imperfect FG-GNPRC beam.

Ying et al. [28] explored the stability of FG-GNPRC microtubes subjected to combined hygrothermal loading while considering elastic substrate interactions. Ahmadi and Rash-Ahmadi [29] analyzed the buckling of porous nanocomposite structures within hygrothermal settings. Employing a higher-order formulation and the differential quadrature technique, Sobhy [30] examined the magneto-hygro-thermomechanical characteristics of sandwich curved beams with functionally graded graphene/aluminum face sheets. Zhao et al. established a unified analytical approach to analyze the dynamic performance of porous composite arches [31], as well as FG-GNPRC sandwich shallow shells [32], both under hygrothermal exposure. Oun et al. [33] assessed the hygrothermal durability of GNP-enhanced composites during accelerated aging tests. Mishra and Singh [34] explored the effectiveness of GNP surface treatments on carbon fiber reinforcements for augmenting the moisture-thermal degradation resistance of fiber/epoxy composite structures. By means of the FSDT and HSDT, She et. al carried out the nonlinear dynamic analysis for graphene-reinforced composite plate. Zhang et al. [38] assessed the aeroelastic stability under supersonic airflow for lattice-core sandwich panels with FG-GNPRC skins in hygrothermal environments. The dynamic analysis of cylindrical sandwich shells incorporating graphene-reinforced face layers in hygrothermal environment was performed by Zhang et al. [39]. Yao et al. [40] proposed a pre-twisted blade model for dynamic analysis, while Niu et al. [41] studied the dynamic performance of rotating pretwisted FG-GNPRC cylindrical panels. An et al. [42] studied the natural vibrations of a variable-thickness FG-

GNPRC trapezoidal plate with a perovskite surface layer. In terms of the nonlinear energy sink, Wang et al. [43] studied nonlinear flutter characteristics of porous sandwich conical shells. Wan et al. [44] analyzed the dynamic behavior of hinged trapezoidal FG-GNPRC magneto-electro-elastic sandwich structures with non-uniform thickness.

An examination of current academic literature indicates that CPT, FSDT and HSDT are utilized to study the hygrothermal behaviors of FG-GNPRC systems due to their numerical efficiency and mathematical simplicity. However, conventional methodologies exhibit certain theoretical limitations regarding their inability to account for the zig-zag phenomenon, thereby losing the capacity to precisely illustrate the interlaminar strain distribution features in FG-GNPRC systems [45]. The mechanical performance of FG-GNPRC plates under hygrothermal excitation is more intricate than under mechanical loading, which is triggered by two integrated impacts: the abrupt variation in material properties through the thickness, caused by the functionally graded design; the multi-scale interaction effect induced by the non-uniform distribution of hygrothermal fields. Recent studies on functionalized nanocomposites [46-48] show that adding nanoparticles and changing surface chemistry alter interfacial interactions and multiphysics coupling. These changes affect structural stability and stress transfer from the micro scale to the macro scale. The results show that interface design plays an important role in controlling thermo-hygro-mechanical behavior in advanced composite materials. The research findings of [49-52] have confirmed that transverse normal strain is a key kinematic parameter to achieve accurate thermoelastic stress prediction of composite structure. Nevertheless, existing analytical expressions still need to add transverse normal deformation components through extra displacement parameters, thereby increasing the system dimensionality and computational complexity. To address these deficiencies in analysis and improve the reliability of interfacial-stress prediction for FG-GNPRC structure under a combination of moisture and temperature load; therefore, an all-encompassing computational model should be proposed. The form should strike a balance between accuracy and computational requirements simultaneously. Based on this study, a novel laminated plate framework with transverse normal hygrothermal strain effects is proposed to establish rigorous interface stress evaluations under hygrothermal conditions for FG-GNPRC panels. Theoretical progress is made through two innovative elements; first, although the original displacement parameter was considered while taking account of transverse deformation in the kinematic assumptions, hygrothermal load should be included in the generalized force vector. second, a novel transverse shear stress field is formulated to satisfy interlaminar continuity requirements and account for hygrothermal effects. The proposed model shows significant improvements and passes the prediction performance evaluation test successfully. Efficacy is verified by exist model; then the comparison analysis will be made with the 3D reference solution and classical high-order shear-deformation theories. Multivariate comprehensive sensitivity analysis of parameter changes on the hygrothermal performance responses of plates. The comparison of the proposed solution with reference values shows good conformity to it in terms of solving for inter-laminar shear stresses. Computational architecture has laid out a validated platform for interlaminar stress prediction under complicated hygrothermal circumstance. The developed formula overcomes the persistent dilemma of the aforementioned model complexity and accuracy of the solution, and provides analytical capability for more advanced composite systems in such an environment.

2. Theoretical equations

2.1. Property definition of the GNP-reinforced material

Geometric specifications of the FG-GNPRC panel (Length=b, Width=a, Thickness=h) are presented in Fig. 1. Graphene reinforcement adopts the piecewise gradation technique [8], with volume concentrations fluctuating across individual layers throughout the thickness. Four distinct gradation schemes are investigated:

UD (Uniform): Consistent 0.07 vol% graphene throughout 10 layers: $[(0.07)_{10}]$;

FG-V: Steady decline from 11 vol% (upper) to 3 vol% (lower): $[(0.11)_2/(0.09)_2/(0.07)_2/(0.05)_2/(0.03)_2]$;
FG-O: Symmetrical profile, peak (11 vol%) at mid-plane: $[(0.03/0.05/0.07/0.09/0.11)_s]$.

FG-X: Symmetrical profile, peak minimum (3 vol%) at mid-plane: $[(0.11/0.09/0.07/0.05/0.03)_s]$.

The orthotropic mechanical properties (E_{11}, E_{22}, G_{12}) of nanocomposites are estimated via the advanced Halpin-Tsai procedure [8], which are given by

$$\begin{aligned}
E_{11} &= \delta_1 \frac{1 + 2(a_G/t_G)\psi_1^G V_G E_M}{1 - \psi_1^G V_G} \\
E_{22} &= \delta_2 \frac{1 + 2(a_G/t_G)\psi_2^G V_G E_M}{1 - \psi_2^G V_G} \\
G_{12} &= \delta_3 \frac{G_M}{1 - \psi_{12}^G V_G}
\end{aligned} \tag{1}$$

In the present model, G denotes graphene, while M represents the matrix. The matrix is characterized by its Young's modulus, E_M, and shear modulus, G_M. The dimensions of the GNP are a_G (length), b_G (width), and t_G (thickness). The volume fractions are written as V_G and

10.57647/jnsc.2026.1605.23

matrix V_M, and their sum is equal to 1. The $\delta_i (i = 1,2,3)$ terms represent the efficiency parameters of graphene. The ψ_1^G, ψ_2^G, and ψ_{12}^G are given by

$$\psi_1^G = \frac{E_{11}^G/E_M - 1}{E_{11}^G/E_M + 2a_G/t_G}$$
$$\psi_2^G = \frac{E_{22}^G/E_M - 1}{E_{22}^G/E_M + 2b_G/t_G} \tag{2}$$
$$\psi_{12}^G = \frac{G_{12}^G/E_M - 1}{G_{12}^G/E_M}$$

It should be noted that the extended Halpin-Tsai model adopted herein is based on the ideal assumption of uniform GNP dispersion. However, experimental studies indicate that agglomeration may occur at high GNP contents (typically>0.10 vol%), which can lead to actual effective moduli lower than theoretical predictions. Therefore, for the high-volume-fraction cases (V_G=0.11) involved in this study, the model-predicted mechanical properties may represent an ideal upper bound. Future work will integrate micromechanical models considering agglomeration effects to obtain more accurate material property inputs.

The coefficients for thermal expansion (α_{11}, α_{22}) and moisture expansion (β_{11}, β_{22}) as well as Poisson's ratios (v_{12}) are formally defined through the following relations.

$$\alpha_{11} = \frac{V_M E_M \alpha_M + V_G E_{11}^G \alpha_{11}^G}{V_M E_M + V_G E_{11}^G}$$
$$\alpha_{22} = (1 + v_M) V_M \alpha_M + (1 + v_{12}^G) V_G \alpha_{22}^G - v_{12}\alpha_{11}$$
$$\beta_{11} = \frac{V_M E_M \beta_M + V_G E_{11}^G \beta_{11}^G}{V_M E_M + V_G E_{11}^G} \tag{3}$$
$$\beta_{22} = (1 + v_M) V_M \beta_M + (1 + v_{12}^G) V_G \beta_{22}^G - v_{12}\beta_{11}$$
$$v_{12} = V_G v_{12}^G + V_M v_M$$

The thermal expansion coefficients, moisture expansion coefficients, and Poisson's ratios of the graphene nanoplatelets and the matrix are denoted by (α_{11}^G, α_{22}^G, α_M) , (β_{11}^G, β_{22}^G , β_M), and (v_{12}^G , v_M); respectively.

2.2. Transverse deformation in the normal direction

The 3D elasticity analysis reported in [53] showed that hygrothermal loading induces significant through-thickness gradients in transverse displacement (w) for moderately thick to thick laminated composites. This occurs when hygrothermally generated strains become substantial.

Conventional approaches to improve thermoelastic accuracy typically expand the transverse displacement field using higher-order polynomials, which introduces additional unknown variables. A novel kinematic enrichment strategy addresses this differently: Instead of increasing variables, we suggest a transverse displacement pattern that considers hygrothermal-induced normal strains. This approach maintains the initial count of displacement parameters while incorporating the physics of hygrothermal growth. The elevation of temperature (ΔT) and the elevation of moisture (ΔC) distributions are split into distinct in-plane and through-thickness parts:

$$\Delta T(x,y,z) = j(z)T(x,y)$$
$$\Delta C(x,y,z) = k(z)C(x,y) \tag{4}$$

where, $T(x, y)$ represents the plane-wise thermal and humidity density patterns, whereas $j(z)$ and $k(z)$ control the vertical thermal and moisture density gradient distributions, being specified as

$$j(z) = j_1(z) + j_2(z) + j_3(z)$$
$$k(z) = k_1(z) + k_2(z) + k_3(z) \tag{5}$$

in which $j_1(z) = k_1(z) = 1$, $j_2(z) = k_2(z) = 2z/h$, $j_3(z) = k_3(z) = G_z/h$, $G_z = (h/\pi)\sin(\pi z/h)$.

The lateral displacement $w_{HT}^k(x,y,z)$ is shown as

$$w_{HT}^k(x,y,z) = \Xi^k(z)T(x,y) + \bar{\Xi}^k(z)C(x,y) \tag{6}$$

Where

$$\Xi^k(z) = \int_0^z \alpha_z^k j(z)dz$$
$$\bar{\Xi}^k(z) = \int_0^z \beta_z^k k(z)dz \tag{7}$$

where α_z^k and β_z^k denote the thermal and moisture expansion modulus along the z-axis at the kth-ply, individually. The lateral deflection is derived via in terms of the stress-strain relationship, in which elastic compliance contributions are omitted to distinguish the unique impact of moisture-thermal loading. Thus, the lateral displacement may be shown as

$$w^k(x,y,z) = w_0(x,y) + w_{HT}^k(x,y,z) \tag{8}$$

where W_0 represents the lateral deflection at mid-plane.

2.3. Assumed displacement field

The spatial motion distribution within a composite plate is developed via superposition, combining two distinct kinematic formulations: a third-order global displacement field that captures the macroscopic continuum response, along with superimposed local displacement terms that provides localized refinements. This formulation is expressed as:

$$\begin{aligned} u^k(x,y,z) &= u_0(x,y) + \sum_{i=1}^{3} z^i u_i(x,y) + \hat{u}_L^k(x,y,z) \\ v^k(x,y,z) &= v_0(x,y) + \sum_{i=1}^{3} z^i v_i(x,y) + \hat{v}_L^k(x,y,z) \\ w^k(x,y,z) &= w_0(x,y) + w_{HT}^k(x,y,z) \end{aligned} \tag{9}$$

where, u_0 and v_0 represent the in-plane uniform displacements, w_0 signifies the steady lateral normal displacement variable within the central plane, while w_{HT}^k stands for the lateral normal movement resulting from variations in thermal conditions and humidity levels, u_1 and v_1 are the bending rotations, while u_2, u_3, v_2, v_3 represent the higher-order parameters. The local displacement variables $\overline{u}_L^k$ and $\overline{v}_L^k$ are assumed as

$$\begin{aligned} \overline{u}_L^k(x,y,z) &= M^k(z) u_L(x,y) \\ \overline{v}_L^k(x,y,z) &= M^k(z) v_L(x,y) \end{aligned} \tag{10}$$

herein, $M^k(z) = (-1)^k \xi_k$denotes the Murakami local displacement variable [54], a methodology developed for simulating the zigzag deformations within layered composite systems. $\xi_k = a_k z - b_k$, $a_k = 2/h_k$, $b_k = (z_{k+1} + z_k)/h_k$, while$h_k$represents the thickness of kth layer, z_k is illustrated in Fig. 1.

The interlaminar shear stresses is given by

$$\begin{aligned} \tau_{xz}^k &= Q_{44}^k \gamma_{xz}^k \\ \tau_{yz}^k &= Q_{55}^k \gamma_{yz}^k \end{aligned} \tag{11}$$

in which

$$\begin{aligned} \gamma_{xz}^k &= w_{0,x} + \Xi^k(z) T_{,x} + \overline{\Xi}^k(z) C_{,x} + u_1 + 2z u_2 + 3z^2 u_3 + (-1)^k a_k u_L \\ \gamma_{yz}^k &= w_{0,y} + \Xi^k(z) T_{,y} + \overline{\Xi}^k(z) C_{,y} + v_1 + 2z v_2 + 3z^2 v_3 + (-1)^k a_k v_L \end{aligned} \tag{12}$$

The edge constraints associated with zero shear force are enforced on each upper and lower faces, as specified by Introducing Eqs. (11) ~ (12) into Eq. (13), leads to

$$\begin{aligned} &\tau_{xz}^1(z_1)=0,\ \tau_{xz}^N(z_{N+1})=0 \\ &\tau_{yz}^1(z_1)=0,\ \tau_{yz}^N(z_{N+1})=0 \end{aligned} \tag{13}$$

$$\begin{aligned} &w_{0,x}+\Xi^1(z_1)T_{,x}+\overline{\Xi}^1(z_1)C_{,x} \\ &+u_1+2z_1u_2+3z_1^2u_3+(-1)^1a_1u_L=0 \\ &w_{0,x}+\Xi^N(z_{N+1})T_{,x}+\overline{\Xi}^N(z_{N+1})C_{,x} \\ &+u_1+2z_{N+1}u_2+3z_{N+1}^2u_3+(-1)^Na_Nu_L=0 \\ &w_{0,y}+\Xi^1(z_1)T_{,y}+\overline{\Xi}^1(z_1)C_{,y} \\ &+v_1+2z_1v_2+3z_1^2v_3+(-1)^1a_1v_L=0 \\ &w_{0,y}+\Xi^N(z_{N+1})T_{,y}+\overline{\Xi}^N(z_{N+1})C_{,y} \\ &+v_1+2z_{N+1}v_2+3z_{N+1}^2v_3+(-1)^Na_Nv_L=0 \end{aligned} \tag{14}$$

In terms of the Eq. (14), obtained

$$\begin{aligned} u_2 &= \frac{(-1)^1a_1-(-1)^Na_{N+1}}{2h}u_L + \frac{\Xi^1(z_1)-\Xi^N(z_{N+1})}{2h}T_{,x} + \frac{\overline{\Xi}^1(z_1)-\overline{\Xi}^N(z_{N+1})}{2h}C_{,x} \\ v_2 &= \frac{(-1)^1a_1-(-1)^Na_{N+1}}{2h}v_L + \frac{\Xi^1(z_1)-\Xi^N(z_{N+1})}{2h}T_{,y} + \frac{\overline{\Xi}^1(z_1)-\overline{\Xi}^N(z_{N+1})}{2h}C_{,y} \end{aligned} \tag{15}$$

Substituting Eq. (15) into Eq. (9), leads to

$$\begin{aligned} u &= u_0 + \Phi_1^k u_1 + \Phi_2^k u_3 + \Phi_3^k u_L + \Phi_4^k \frac{\partial T}{\partial x} + \Phi_5^k \frac{\partial C}{\partial x} \\ v &= v_0 + \Psi_1^k v_1 + \Psi_2^k v_3 + \Psi_3^k v_L + \Psi_4^k \frac{\partial T}{\partial y} + \Psi_5^k \frac{\partial C}{\partial y} \\ w &= w_0 + w_{HT}^k \end{aligned} \tag{16}$$

$$\begin{Bmatrix} \Phi_1 & \Psi_1 \\ \Phi_2 & \Psi_2 \\ \Phi_3 & \Psi_3 \\ \Phi_4 & \Psi_4 \\ \Phi_5 & \Psi_5 \end{Bmatrix} = \begin{bmatrix} z & z \\ z^3 & z^3 \\ M^k(z) + \left(\frac{(-1)^1a_1-(-1)^Na_{N+1}}{2h}\right)z^2 & M^k(z) + \left(\frac{(-1)^1a_1-(-1)^Na_{N+1}}{2h}\right)z^2 \\ \left(\frac{\Xi^1(z_1)-\Xi^N(z_{N+1})}{2h}\right)z^2 & \left(\frac{\Xi^1(z_1)-\Xi^N(z_{N+1})}{2h}\right)z^2 \\ \left(\frac{\bar{\Xi}^1(z_1)-\bar{\Xi}^N(z_{N+1})}{2h}\right)z^2 & \left(\frac{\bar{\Xi}^1(z_1)-\bar{\Xi}^N(z_{N+1})}{2h}\right)z^2 \end{bmatrix} \tag{17}$$

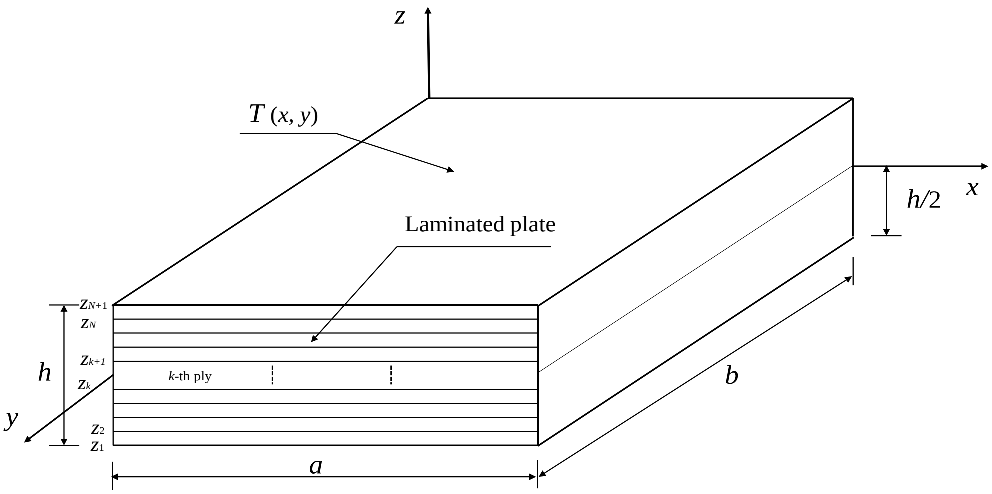

Figure 1. Geometry of the composite plate cross section

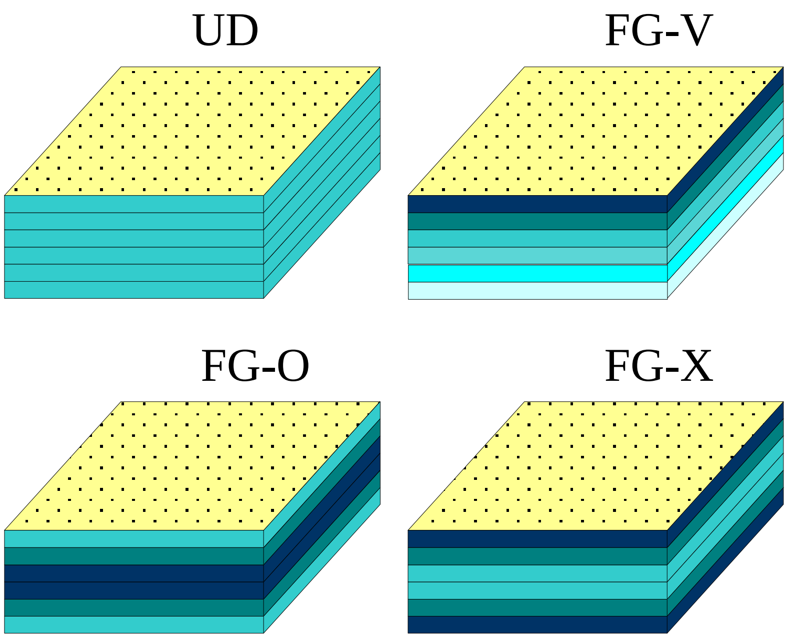

Figure 2. Four GNP patterns of FG-GNPRC plates

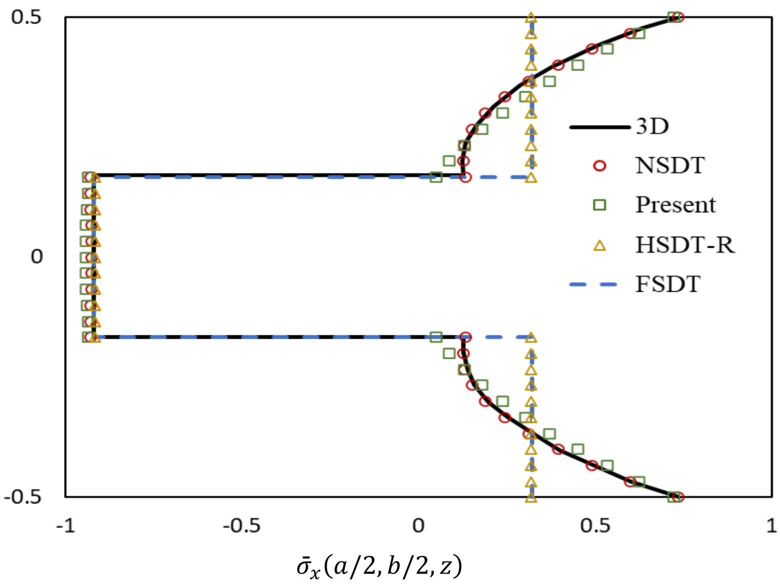

Figure 3. In-plane stress profiles of the 3-layer composite plate (a/h=5)

10.57647/jnsc.2026.1605.23

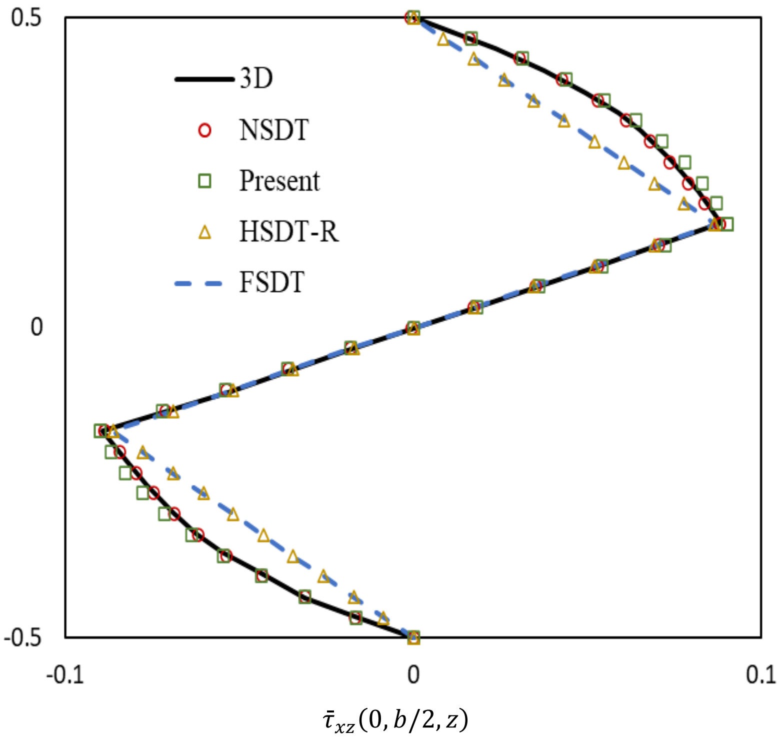

Figure 4. Transverse shear stress profiles of the 3-layer composite plate (*a*/*h*=5)

Based on the displacement distribution of the suggested model, the strain parameters are expressed as

$$
\begin{aligned}
\varepsilon_x^k &= \frac{\partial u_0}{\partial x} + \Phi_1^k \frac{\partial u_1}{\partial x} + \Phi_2^k \frac{\partial u_3}{\partial x} \\
&\quad + \Phi_3^k \frac{\partial u_L}{\partial x} + \Phi_4^k \frac{\partial^2 T}{\partial x^2} + \Phi_5^k \frac{\partial^2 C}{\partial x^2} \\
\varepsilon_y^k &= \frac{\partial v_0}{\partial y} + \Psi_1^k \frac{\partial v_1}{\partial y} + \Psi_2^k \frac{\partial v_3}{\partial y} \\
&\quad + \Psi_3^k \frac{\partial v_L}{\partial y} + \Psi_4^k \frac{\partial^2 T}{\partial y^2} + \Psi_5^k \frac{\partial^2 C}{\partial y^2} \\
\gamma_{xy}^k &= \frac{\partial u_0}{\partial y} + \frac{\partial v_0}{\partial x} + \Phi_1^k \frac{\partial u_1}{\partial y} + \Psi_1^k \frac{\partial v_1}{\partial x} + \Phi_2^k \frac{\partial u_3}{\partial y} + \Psi_2^k \frac{\partial v_3}{\partial x} \\
&\quad + \Phi_3^k \frac{\partial u_L}{\partial y} + \Psi_3^k \frac{\partial v_L}{\partial x} + (\Phi_4^k + \Psi_4^k) \frac{\partial^2 T}{\partial x \partial y} + (\Phi_5^k + \Psi_5^k) \frac{\partial^2 C}{\partial x \partial y}
\end{aligned}
\tag{18}
$$

$$
\begin{aligned}
\gamma_{xz}^k &= \frac{\partial w_0}{\partial x} + \frac{\partial \Phi_1^k}{\partial z} u_1 + \frac{\partial \Phi_2^k}{\partial z} u_3 + \frac{\partial \Phi_3^k}{\partial z} u_L \\
&\quad + \left(\frac{\partial \Phi_4^k}{\partial z} + \Xi^k(z)\right) \frac{\partial T}{\partial x} + \left(\frac{\partial \Phi_5^k}{\partial z} + \Xi^k(z)\right) \frac{\partial C}{\partial x} \\
\gamma_{yz}^k &= \frac{\partial w_0}{\partial y} + \frac{\partial \Psi_1^k}{\partial z} v_1 + \frac{\partial \Psi_2^k}{\partial z} v_3 + \frac{\partial \Psi_3^k}{\partial z} v_L \\
&\quad + \left(\frac{\partial \Psi_4^k}{\partial z} + \Xi^k(z)\right) \frac{\partial T}{\partial y} + \left(\frac{\partial \Psi_5^k}{\partial z} + \Xi^k(z)\right) \frac{\partial C}{\partial y}
\end{aligned}
$$

The fundamental expression for the stress-strain connection of the laminated plate under combined thermal-humidity loading is presented as:

$$
\begin{Bmatrix} \sigma_x \\ \sigma_y \\ \tau_{xy} \\ \tau_{xz} \\ \tau_{yz} \end{Bmatrix}^k =
\begin{bmatrix} Q_{11} & Q_{12} & 0 & 0 & 0 \\ Q_{21} & Q_{22} & 0 & 0 & 0 \\ 0 & 0 & Q_{33} & 0 & 0 \\ 0 & 0 & 0 & Q_{44} & 0 \\ 0 & 0 & 0 & 0 & Q_{55} \end{bmatrix}^k
\begin{Bmatrix} \varepsilon_x - \alpha_x \Delta T - \beta_x \Delta T \\ \varepsilon_y - \alpha_y \Delta T - \beta_y \Delta T \\ \gamma_{xy} - \alpha_{xy} \Delta T - \beta_{xy} \Delta T \\ \gamma_{xz} \\ \gamma_{yz} \end{Bmatrix}^k
\tag{19}
$$

wherein the symbol Q_{ij}^k represents the modified stiffness parameters for the *k*th layer, whereas α_x^k, α_y^k and α_{xy}^k denote the thermal expansion metrics for the coordinate directions of the *k*th layer, and β_x^k, β_y^k and β_{xy}^k signify the moisture expansion factors for the *k*th layer of plate.

2.4. Novel interlaminar shear stress field

Regarding the evaluation of multilayered composite plates, the determination of through-thickness shear stresses utilizing constitutive laws might produce less accurate results. To improve the reliability, the three-dimensional elasticity equations together with the Reissner mixed variational principle (RMVP) [55] are utilized. A distinct feature of this current methodology is its improved accuracy in identifying the interlaminar shear stresses.By disregarding body and inertial forces, the three-dimensional elasticity equations can be formulated as follows

$$\begin{aligned}&\frac{\partial\sigma_x^k}{\partial x}+\frac{\partial\tau_{xy}^k}{\partial y}+\frac{\partial\tau_{xz}^k}{\partial z}=0\\&\frac{\partial\sigma_y^k}{\partial y}+\frac{\partial\tau_{xy}^k}{\partial x}+\frac{\partial\tau_{yz}^k}{\partial z}=0\end{aligned}\tag{20}$$

By incorporating Eq. (20) across the thickness dimension and applying the given constraint $\tilde{\tau}_{xz}^k(z_1)=0$ and $\tilde{\tau}_{yz}^k(z_1)=0$, results in

$$\begin{aligned}&\tilde{\tau}_{xz}^k(x,y,z)=-\int_{z_1}^{z}\left[\frac{\partial\sigma_x^k}{\partial x}+\frac{\partial\tau_{xy}^k}{\partial y}\right]dz\\&\tilde{\tau}_{yz}^k(x,y,z)=-\int_{z_1}^{z}\left[\frac{\partial\sigma_y^k}{\partial y}+\frac{\partial\tau_{xy}^k}{\partial x}\right]dz\end{aligned}\tag{21}$$

By substituting Eqs. (16)-(19) into Eq. (21), several second-order partial derivatives are obtained. For cross-ply structures, balancing precision against computational speed, a reduced form of transverse shear stress terms is utilized in Eq. (21), as presented below

$$\begin{aligned}&\tilde{\tau}_{xz}^k(x,y,z)=-C_{ZX}U_X-C_{XHT}U_{XHT}\\&\tilde{\tau}_{xz}^k(x,y,z)=-C_{ZY}U_Y-C_{YHT}U_{YHT}\end{aligned}\tag{22}$$

Where

$$\begin{aligned}&C_{ZX}=\int_{z_1}^{z}Q_{11}^k[1\quad \Phi_1^k\quad \Phi_2^k\quad \Phi_3^k]\,dz\\&C_{ZY}=\int_{z_1}^{z}Q_{22}^k[1\quad \Psi_1^k\quad \Psi_2^k\quad \Psi_3^k]\,dz\\&U_X=[u_{0,xx}\quad u_{1,xx}\quad u_{3,xx}\quad u_{L,xx}]^T\\&U_Y=[v_{0,yy}\quad v_{1,yy}\quad v_{3,yy}\quad v_{L,yy}]^T\end{aligned}\tag{23}$$

$$\begin{aligned}&C_{XHT}\\&=\int_{z_1}^{z}Q_{11}^k[\Phi_4^k\quad -\alpha_x f(z)\quad \Phi_5^k\quad -\beta_x g(z)]\,dz\\&C_{YHT}\\&=\int_{z_1}^{z}Q_{22}^k[\Psi_4^k\quad -\alpha_y f(z)\quad \Psi_5^k\quad -\beta_y g(z)]\,dz\\&U_{XHT}=[T_{,xxx}\quad T_{,x}\quad C_{,xxx}\quad C_{,x}]^T\\&U_{YHT}=[T_{,yyy}\quad T_{,y}\quad C_{,yyy}\quad C_{,y}]^T\end{aligned}\tag{24}$$

Applying the condition $\tilde{\tau}_{xz}^k(z_{N+1})=0$ and $\tilde{\tau}_{yz}^k(z_{N+1})=0$, the following equations are derived

$$\begin{aligned}&\tilde{\tau}_{xz}^k(x,y,z)=E_{ZX}\bar{U}_X+E_{XHT}U_{XHT}\\&\tilde{\tau}_{yz}^k(x,y,z)=E_{ZY}\bar{U}_Y+E_{YHT}U_{YHT}\end{aligned}\tag{25}$$

$$\begin{aligned}&E_{ZX}=\frac{C_{ZX}^{(1)}(z)}{C_{ZX}^{(1)}(z_1)}\tilde{C}_{ZX}(z_{N+1})-\tilde{C}_{ZX}(z)\\&E_{ZY}=\frac{C_{ZY}^{(1)}(z)}{C_{ZY}^{(1)}(z_1)}\tilde{C}_{ZY}(z_{N+1})-\tilde{C}_{ZY}(z)\end{aligned}\tag{26}$$

$$\bar{U}_Y=[v_{1,yy}\quad v_{3,yy}\quad v_{L,yy}]^T$$

$$\begin{aligned}&E_{XHT}=\frac{C_{ZX}^{(1)}(z)}{C_{ZX}^{(1)}(z_1)}C_{XHT}(z_{N+1})-C_{XHT}(z)\\&E_{YHT}=\frac{C_{ZY}^{(1)}(z)}{C_{ZY}^{(1)}(z_1)}C_{YHT}(z_{N+1})-C_{YHT}(z)\end{aligned}\tag{27}$$

in which

$$\begin{aligned}&\tilde{C}_{ZX}(z)=\{C_{ZX}^{(2)}(z)\quad C_{ZX}^{(3)}(z)\quad C_{ZX}^{(4)}(z)\}\\&\tilde{C}_{ZY}(z)=\{C_{ZY}^{(2)}(z)\quad C_{ZY}^{(3)}(z)\quad C_{ZY}^{(4)}(z)\}\end{aligned}\tag{28}$$

where $C_{ZX}^{(1)}(z)$ and $C_{ZY}^{(1)}(z)$ are the ith elements of the $C_{ZX}(z)$ and $C_{ZY}(z)$, respectively.

Eq. (22) demonstrates that the formulation for transverse shear stress includes second-order derivatives of displacement variables, presenting difficulties during the finite element modeling process. To overcome this difficulty, the RMVT [55] provides a procedure to remove the $\overline{U}_x$ and $\overline{U}_y$, $\bar{\mathbf{U}}_y$, which is given by

$$\begin{aligned}\delta\Pi_R=\int_{S_m}\int_{-h/2}^{h/2}&[\sigma_x^k\delta\varepsilon_x^k+\sigma_y^k\delta\varepsilon_y^k+\tau_{xy}^k\delta\gamma_{xy}^k\\&+\tilde{\tau}_{xz}^k\delta\gamma_{xz}^k+\tilde{\tau}_{yz}^k\delta\gamma_{yz}^k+\\&\delta\tilde{\tau}_{xz}^k(\gamma_{xz}^k-\tilde{\gamma}_{xz}^k)+\delta\tilde{\tau}_{yz}^k(\gamma_{yz}^k-\tilde{\gamma}_{yz}^k)]dzdxdy\\&-\delta W_e=0\end{aligned}\tag{29}$$

where W_e signifies the work performed by the applied forces acting on the plate. Additionally, $\hat{\gamma}_{xz}^k$ and $\hat{\gamma}_{yz}^k$ denote the transverse shear strain that is relation to the $\tilde{\tau}_{xz}^k$ and $\tilde{\tau}_{yz}^k$, $\hat{\gamma}_{xz}^k=\tilde{\tau}_{xz}^k/Q_{44}^k$, $\hat{\gamma}_{yz}^k=\tilde{\tau}_{yz}^k/Q_{55}^k$.

Significantly, the $\tilde{\tau}_{xz}^k$ and $\tilde{\tau}_{yz}^k$ do not utilize displacement parameters, which permits the variational formulation established in Eq. (29) to be executed through a two-phase methodology.

$$\begin{aligned}\int_{S_m}\int_{-h/2}^{h/2}&(\sigma_x^k\delta\varepsilon_x^k+\sigma_y^k\delta\varepsilon_y^k+\tau_{xy}^k\delta\gamma_{xy}^k\\&+\tilde{\tau}_{xz}^k\delta\gamma_{xz}^k\\&+\tilde{\tau}_{yz}^k\delta\gamma_{yz}^k)dzdxdy-\delta W_e\\&=0\end{aligned}\tag{30}$$

$$\begin{aligned}\int_{S_m}\int_{-h/2}^{h/2}&(\delta\tilde{\tau}_{xz}^k(\gamma_{xz}^k-\tilde{\gamma}_{xz}^k)+\delta\tilde{\tau}_{yz}^k(\gamma_{yz}^k\\&-\tilde{\gamma}_{yz}^k))dzdxdy=0\end{aligned}\tag{31}$$

Inserting Eqs. (18) and (25) into Eq. (31), the following equation is obtained

10.57647/jnsc.2026.1605.23

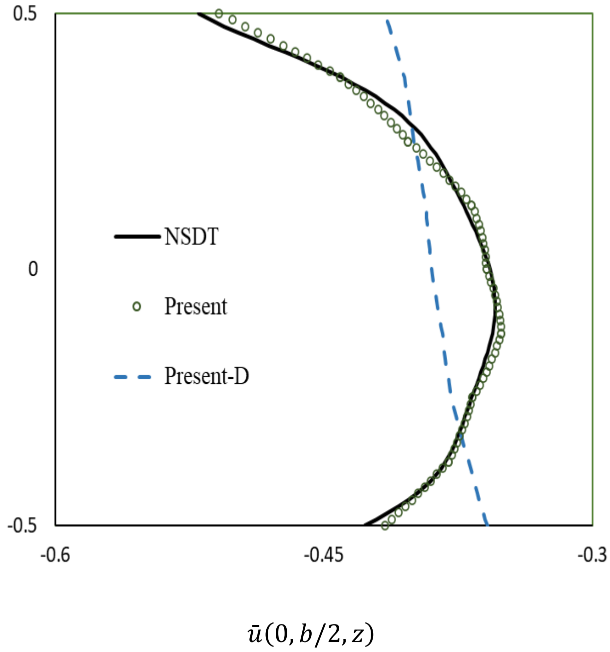

Figure 5. In-plane displacement profiles of the 8-layer composite plate (*a/h*=5)

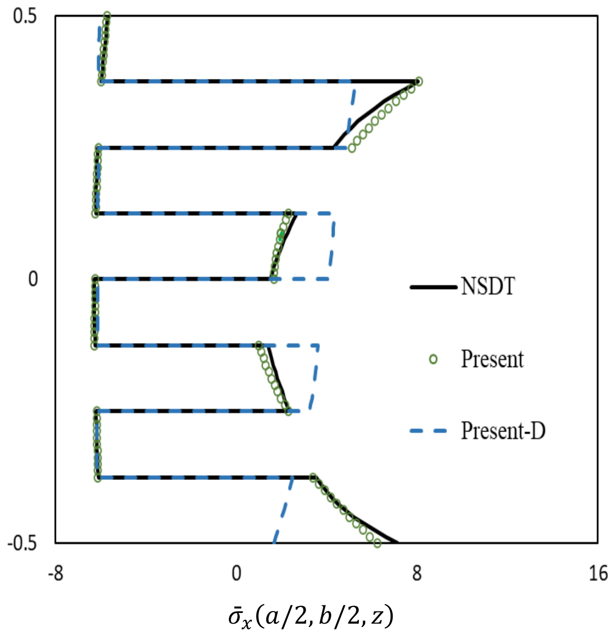

Figure 6. In-plane stress profiles of the 8-layer composite plate (*a/h*=5)

Where

$$\int_{-h/2}^{h/2} \delta \overline{U}_X^T E_{ZX}^T \begin{pmatrix} B_{XZ}G_{XZ} + \left(\Phi_{4,z}^k + \overline{\Xi}^k(z)\right)T_{,x} \\ +\left(\Phi_{5,z}^k + \overline{\overline{\Xi}}^k(z)\right)C_{,x} \\ -E_{ZX}\overline{U}_X/Q_{44}^k - E_{XHT}\,\overline{U}_{XHT}/Q_{44}^k \end{pmatrix} dz = 0$$
$$\int_{-h/2}^{h/2} \delta \overline{U}_Y^T E_{ZY}^T \begin{pmatrix} B_{YZ}G_{YZ} + \left(\Psi_{4,z}^k + \overline{\Xi}^k(z)\right)T_{,y} \\ +\left(\Psi_{5,z}^k + \overline{\overline{\Xi}}^k(z)\right)C_{,y} \\ -E_{ZY}\overline{U}_Y/Q_{55}^k - E_{YHT}\,\overline{U}_{YHT}/Q_{55}^k \end{pmatrix} dz = 0 \quad (32)$$

$$\mathbf{B}_{XZ}=\left\{\Phi_{1,z}^k \quad \Phi_{2,z}^k \quad \Phi_{3,z}^k \quad 1\right\}$$
$$\mathbf{B}_{YZ}=\left\{\Psi_{1,z}^k \quad \Psi_{2,z}^k \quad \Psi_{3,z}^k \quad 1\right\} \quad (33)$$

$$\mathbf{G}_{XZ}=\left\{u_1 \quad u_3 \quad u_L \quad w_{0,x}\right\}^{\mathrm{T}}$$
$$\mathbf{G}_{YZ}=\left\{v_1 \quad v_3 \quad v_L \quad w_{0,y}\right\}^{\mathrm{T}} \quad (34)$$

Consequently, the second-order derivatives are reorganized as follows

$$\bar{\mathbf{U}}_x = \mathbf{C}_{\mathrm{XE}}\mathbf{G}_{\mathrm{XZ}} + \mathbf{C}_{\mathrm{XEHT}}\mathbf{U}_{\mathrm{XHT}} \qquad (35)$$
$$\bar{\mathbf{U}}_y = \mathbf{C}_{\mathrm{YE}}\mathbf{G}_{\mathrm{YZ}} + \mathbf{C}_{\mathrm{YEHT}}\mathbf{U}_{\mathrm{YHT}}$$

in which

$$C_{XE} = \left[\int_{-\frac{h}{2}}^{h/2} (E_{ZX}^T E_{ZX}/Q_{44}^k)dz\right]^{-1} \left[\int_{-h/2}^{h/2} E_{ZX}^T B_{XZ}dz\right] \qquad (36)$$
$$C_{YE} = \left[\int_{-\frac{h}{2}}^{h/2} (E_{ZY}^T E_{ZY}/Q_{55}^k)dz\right]^{-1} \left[\int_{-h/2}^{h/2} E_{ZY}^T B_{YZ}dz\right]$$

$$C_{XEHT} = \left[\int_{-\frac{h}{2}}^{h/2} (E_{ZX}^T E_{ZX}/Q_{44}^k)dz\right]^{-1} \left[\int_{-h/2}^{h/2} E_{ZX}^T F_{XHT}dz\right] \qquad (37)$$
$$C_{YEHT} = \left[\int_{-\frac{h}{2}}^{h/2} (E_{ZY}^T E_{ZY}/Q_{55}^k)dz\right]^{-1} \left[\int_{-h/2}^{h/2} E_{ZY}^T F_{YHT}dz\right]$$

$$\mathbf{F}_{\mathrm{XHT}} = \begin{Bmatrix} -E_{\mathrm{XHT}}^{(1)}(z)/Q_{44}^k \\ \Phi_{4,x}^k + \Xi^k(z) - E_{\mathrm{XHT}}^{(2)}(z)/Q_{44}^k \\ -E_{\mathrm{XHT}}^{(3)}(z)/Q_{44}^k \\ \Phi_{5,x}^k + \bar{\Xi}^k(z) - E_{\mathrm{XHT}}^{(4)}(z)/Q_{44}^k \end{Bmatrix}^{\mathrm{T}} \qquad (38)$$
$$\mathbf{F}_{\mathrm{YHT}} = \begin{Bmatrix} -E_{\mathrm{YHT}}^{(1)}(z)/Q_{55}^k \\ \Psi_{4,x}^k + \Xi^k(z) - E_{\mathrm{YHT}}^{(2)}(z)/Q_{55}^k \\ -E_{\mathrm{YHT}}^{(3)}(z)/Q_{55}^k \\ \Psi_{5,x}^k + \bar{\Xi}^k(z) - E_{\mathrm{YHT}}^{(4)}(z)/Q_{55}^k \end{Bmatrix}^{\mathrm{T}}$$

where $E_{XHT}^{(j)}(z)$ and $E_{YHT}^{(j)}(z)$ are the jth components of the $E_{XHT}(z)$ and $E_{YHT}(z)$, respectively.

By inserting Eq. (35) into Eq. (25), the ultimate interlayer shear stress distribution is presented as

$$\tilde{\tau}_{xz}^k(x,y,z) = E_{ZX}C_{XE}G_{XZ} + (E_{ZX}C_{XEHT} + E_{XHT})U_{XHT} \qquad (39)$$
$$\tilde{\tau}_{yz}^k(x,y,z) = E_{ZY}C_{YE}G_{YZ} + (E_{ZY}C_{YEHT} + E_{YHT})U_{YHT}$$

Based on the improved interlaminar shear stress field (Eq. 39), high-precision interlaminar shear stresses can be directly calculated, eliminating the need for post-analysis.

2.5. Governing equations

To derive the fundamental equations, Eq. (30) can be restated as

$$\delta U - \delta W = 0 \qquad (40)$$

Which

$$\delta U = \int_{S_m}\int_{-\frac{h}{2}}^{h/2} (\sigma_x^k \delta\varepsilon_x^k + \sigma_y^k \delta\varepsilon_y^k + \tau_{xy}^k \delta\gamma_{xy}^k + \tilde{\tau}_{xz}^k \delta\gamma_{xz}^k + \tilde{\tau}_{yz}^k \delta\gamma_{yz}^k) dxdydz = 0 \qquad (41)$$

$$\delta W = \int_{\Omega}\int_{-h/2}^{h/2} q\delta\, w_0 d\Omega \qquad (42)$$

Substituting Eqs. (16), (18), (19) and (39) into Eq. (41), performing integration by parts, and grouping terms associated with the virtual displacements δu_0, δu_1, δu_3, δu_L, δv_0, $\Delta\delta v_1$, $\Delta\delta v_3$, δv_L and δw_0, results in the governing equations.

3. Solution procedure

This investigation centers on analytical expressions for simply-supported plates.

The geometric boundary conditions are therefore formulated as:

$$\begin{aligned}
&\delta u_0: \sum_{k=1}^{n}\int_{z_k}^{z_{k+1}}\left(\frac{\partial\sigma_x}{\partial x}+\frac{\partial\tau_{xy}}{\partial y}\right)dz=0\\
&\delta u_1: \sum_{k=1}^{n}\int_{z_k}^{z_{k+1}}\left(\Phi_1^k\left(\frac{\partial\sigma_x}{\partial x}+\frac{\partial\tau_{xy}}{\partial y}\right)-\frac{\partial\Phi_1^k}{\partial z}\tilde{\tau}_{xz}\right)dz=0\\
&\delta u_3: \sum_{k=1}^{n}\int_{z_k}^{z_{k+1}}\left(\Phi_2^k\left(\frac{\partial\sigma_x}{\partial x}+\frac{\partial\tau_{xy}}{\partial y}\right)-\frac{\partial\Phi_2^k}{\partial z}\tilde{\tau}_{xz}\right)dz=0\\
&\delta u_L: \sum_{k=1}^{n}\int_{z_k}^{z_{k+1}}\left(\Phi_3^k\left(\frac{\partial\sigma_x}{\partial x}+\frac{\partial\tau_{xy}}{\partial y}\right)-\frac{\partial\Phi_3^k}{\partial z}\tilde{\tau}_{xz}\right)dz=0\\
&\delta v_0: \sum_{k=1}^{n}\int_{z_k}^{z_{k+1}}\left(\frac{\partial\sigma_y}{\partial y}+\frac{\partial\tau_{xy}}{\partial x}\right)dz=0 \qquad (43)\\
&\delta v_1: \sum_{k=1}^{n}\int_{z_k}^{z_{k+1}}\left(\Psi_1^k\left(\frac{\partial\sigma_y}{\partial y}+\frac{\partial\tau_{xy}}{\partial x}\right)-\frac{\partial\Psi_1^k}{\partial z}\tilde{\tau}_{yz}\right)dz=0\\
&\delta v_3: \sum_{k=1}^{n}\int_{z_k}^{z_{k+1}}\left(\Psi_2^k\left(\frac{\partial\sigma_y}{\partial y}+\frac{\partial\tau_{xy}}{\partial x}\right)-\frac{\partial\Psi_2^k}{\partial z}\tilde{\tau}_{yz}\right)dz=0\\
&\delta v_L: \sum_{k=1}^{n}\int_{z_k}^{z_{k+1}}\left(\Psi_3^k\left(\frac{\partial\sigma_y}{\partial y}+\frac{\partial\tau_{xy}}{\partial x}\right)-\frac{\partial\Psi_3^k}{\partial z}\tilde{\tau}_{yz}\right)dz=0\\
&\delta w_0: \sum_{k=1}^{n}\int_{z_k}^{z_{k+1}}\left(\frac{\partial\tilde{\tau}_{xz}}{\partial x}+\frac{\partial\tilde{\tau}_{yz}}{\partial y}\right)dz=0
\end{aligned}$$

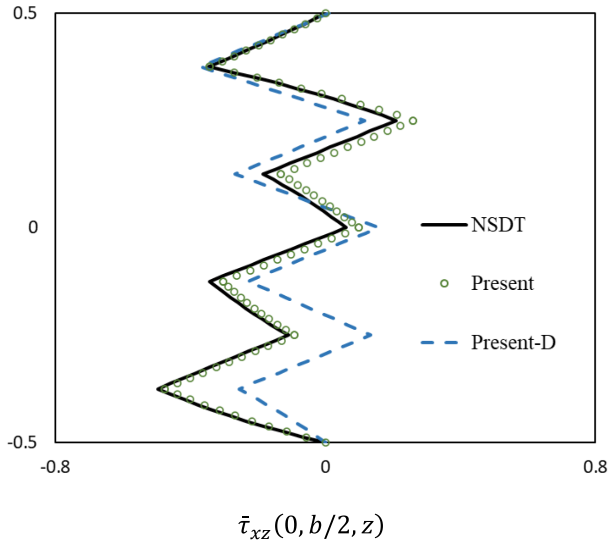

Figure 7. Transverse shear stress profiles of the 8-layer composite plate (*a/h*=5)

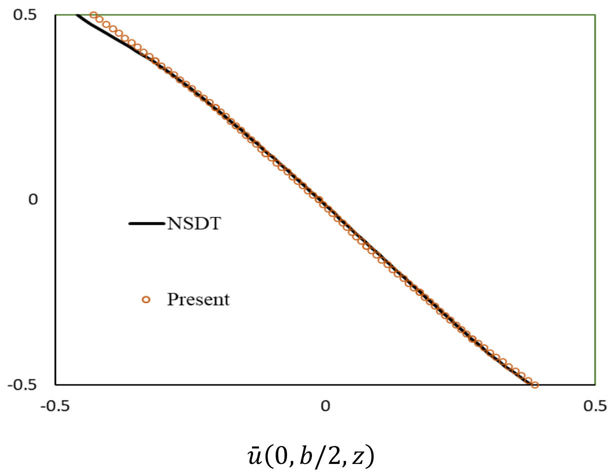

Figure 8. Through-thickness in-plane displacements of the 8-layer composite plate (*a/h*=5)

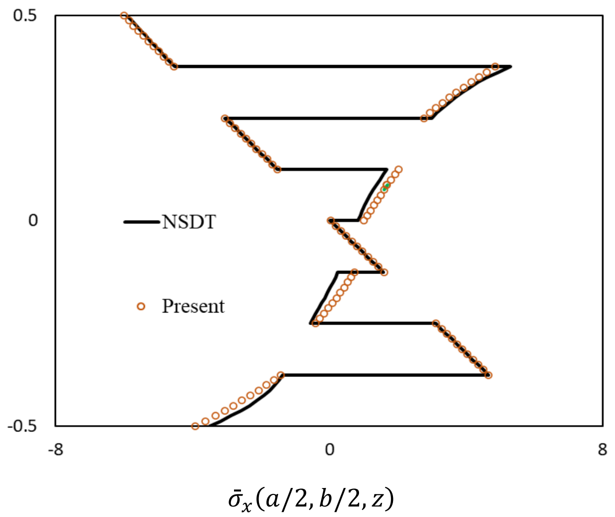

Figure 9. Through-thickness in-plane stresses of the 8-layer composite plate (*a/h*=5

10.57647/jnsc.2026.1605.23

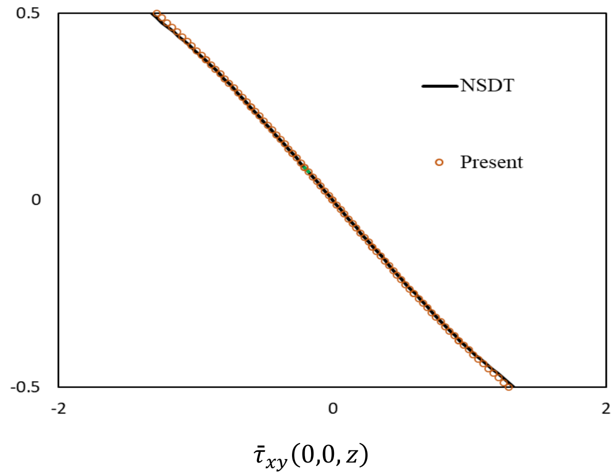

Figure 10. In-plane stress variations in the 8-layer composite plate (*a*/*h*=5)

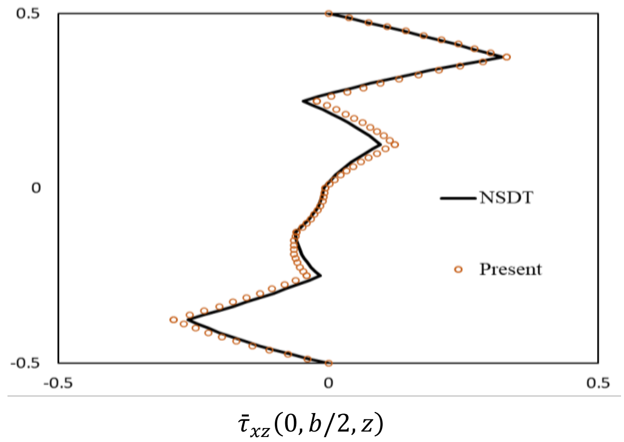

Figure 11. Transverse shear stress variations in the 8-layer composite plate (*a*/*h*=5)

Along the boundaries defined by *x*=0 and *x*=*a*, the corresponding boundary conditions are given by

$$v_0 = v_1 = v_L = w_0 = 0 \tag{44}$$

Along the boundaries defined by *y*=0 and *y*=*b*, the corresponding boundary conditions are given by

$$u_0 = u_1 = u_L = w_0 = 0 \tag{45}$$

Utilizing a semi-analytical Navier-based strategy, the displacement fields meeting the specified constraints are formulated as (46)

$$\begin{aligned}
u_0 &= \sum_{m=1}^{\infty}\sum_{n=1}^{\infty} u_{0mn}\cos\alpha x\sin\beta y & v_0 &= \sum_{m=1}^{\infty}\sum_{n=1}^{\infty} v_{0mn}\sin\alpha x\cos\beta y\\
u_1 &= \sum_{m=1}^{\infty}\sum_{n=1}^{\infty} u_{1mn}\cos\alpha x\sin\beta y & v_1 &= \sum_{m=1}^{\infty}\sum_{n=1}^{\infty} v_{1mn}\sin\alpha x\cos\beta y\\
u_3 &= \sum_{m=1}^{\infty}\sum_{n=1}^{\infty} u_{3mn}\cos\alpha x\sin\beta y & v_3 &= \sum_{m=1}^{\infty}\sum_{n=1}^{\infty} v_{3mn}\sin\alpha x\cos\beta y\\
u_L &= \sum_{m=1}^{\infty}\sum_{n=1}^{\infty} u_{Lmn}\cos\alpha x\sin\beta y & v_L &= \sum_{m=1}^{\infty}\sum_{n=1}^{\infty} v_{Lmn}\sin\alpha x\cos\beta y
\end{aligned}$$

where $\alpha = m\pi/a$, $\beta = n\pi/b$; *a* is the width and denotes the length; *m* and *n* represent the half-wave numbers in the respective directions; u_{0mn}, u_{1mn}, u_{3mn},u_{Lmn}, v_{0mn}, v_{1mn}, v_{3mn}, v_{Lmn} and w_{0mn} represent the primary unknowns. The plate experiences lateral mechanical loading (*q*), thermal loading (Δ*T*), and hygroscopic loading (Δ*C*), assumed to vary as follows

$$q = q_0\sin\alpha x\sin\beta y \tag{47}$$

$$\Delta T = j(z)\sin\alpha x\sin\beta y \tag{48}$$

$$\Delta C = k(z)\sin\alpha x\sin\beta y \tag{49}$$

where q_0 represents the peak intensity of the bi-sinusoidal transverse load.

Analytical expressions for plates on simple supports are derived by inserting Eqs. (46)-(49) into the fundamental governing equation (Eq. 43).

4. Numerical examples and analysis

To evaluate the effectiveness of the current model, numerical simulations regarding FG-GNPRC plates subjected to hygrothermal environments are conducted.

10.57647/jnsc.2026.1605.23

The forecasting capability of the suggested architecture is thoroughly verified against established reference databases and peer-approved numerical standards within composite systems.

4.1. Validation and comparison

This section presents a computational investigation into composite plates subjected to thermal loads $\Delta T = \overline{T}_0 + (2z/h)\overline{T}_1$ ($\overline{T}_i = T_i \sin(\pi x/a)\sin(\pi y/b)$, i=0, 1). The material parameters are [56]: $E_L/E_T = 15$, $G_{LT}/E_T = 0.5$, $G_{TT}/E_T = 0.3356$, $\nu_{LT} = 0.3$, $\nu_{TT} = 0.49$, $E_T = 10\text{GPa}$, $\alpha_L/\alpha_0 = 0.015$, $\alpha_T/\alpha_0 = 1$, $\alpha_0 = 10^{-6}/K$. A symmetric plate (0/90/0) is investigated subjected to a temperature load (T_0=100). The results are normalized through the relations: $(\overline{\sigma}_x, \overline{\tau}_{xz}) = (\sigma_x, \tau_{xz})/(\alpha_0 T_0 E_T)$. Fig. 3 and Fig. 4 provide a comparative evaluation of stress distribution characteristics, involving four theoretical frameworks: the ninth-order theory (NSDT) proposed by Matsunaga [56], Reddy's theory (HSDT-R) [57], the first-order theory (FSDT), and the newly developed model (Present). The NSDT represents the in-plane displacement field through a ninth-order polynomial in the thickness coordinate *z*. Transverse displacement is similarly approximated with an eighth-order polynomial of *z*. The amount of displacement parameters of this formulation needs to be 29. The interlaminar stresses from both the NSDT and other models (HSDT-R, FSDT) are obtained through integration of the 3D elasticity equations, while the interlaminar shear stresses of proposed model is directly calculated from the derived stress field (Eq. 39). Comparative analysis indicates strong agreement between the present model and the 3D solutions [56]. Moreover, the numerical outcomes (NSDT) are also highly consistent with these reference results so that the NSDT results can be used as a reliable reference solution to validate the present theory in the following section. The HSDT-R and FSDT methods, on the other hand, show a decrease in predictive accuracy. This difference is mainly caused by the fact that the models are difficult to account for transverse normal deformation under thermal load conditions. To validate the proposed model more comprehensively, a hygrothermal analysis of the composite plates subjected to hygrothermal loading$\Delta T = \overline{T}_0 + (2z/h)\overline{T}_1$, $\Delta C = \overline{C}_0 + (2z/h)\overline{C}_1$ ($\overline{T}_i = T_i \sin(\pi x/a)\sin(\pi y/b)$, $\overline{C}_i = C_i \sin(\pi x/a)\sin(\pi y/b)$, i=0, 1) is carried out. he results obtained are normalized in accordance with established equations: $\overline{u} = u/(\alpha_0 T_0 a)$, $(\overline{\sigma}_x, \overline{\tau}_{xy}, \overline{\tau}_{xz}, \overline{\tau}_{yz}) = (\sigma_x, \tau_{xy}, \tau_{xz}, \tau_{yz})/(\alpha_0 T_0 E_T)$, i=0, 1. A composite plate with an 8-layer $(0/90)_4$ composite plate stacking sequence under the combined heat and moisture loading condition (T_0=100, C_0=0.001). Comparative evaluation of the displacement and stress distribution in Figs. 5-7 include three modeling methods: the ninth-order higher-order shear deformation theory (NSDT) [56], the Present-D model (excluding the influence of transverse normal deformation) and the fully present formulation (present). Through comparative results can see that the present model has good consistence with benchmark solution (NSDT), while the present-D model is low accuracy of predicting. And what was found in the above higher order deformation is that is further transverse normal deformation. Also, an 8-layer $(0/90)_4$ composite plate is studied under a hygrothermal load (T_1=100, C_1=0.001). Thickness wise displacement and stress distribution comparison shown in Figs. 8-12. Use NSDT solution as references, then through analysis we can see that the present model is consistent with the references data sets. It should be mentioned that the NSDT takes 29 displacement variables, but the present theoretical framework only accepts 9 displacement variables. This difference is the proof of the accuracy and efficiency of the proposed model.

4.2. Parametric study

Parametric studies are carried out to analyze the hygrothermal responses of FG-GNPRC plates subjected to hygrothermal loads ($\Delta T = j_1(z)\overline{T}_0 + j_2(z)\overline{T}_1 + j_3(z)\overline{T}_2$, $\Delta C = k_1(z)\overline{C}_0 + k_2(z)\overline{C}_1 + k_3(z)\overline{C}_2$, $\overline{T}_i = T_i \sin(\pi x/a)\sin(\pi y/b)$, $\overline{C}_i = C_i \sin(\pi x/a)\sin(\pi y/b)$, i=0, 1, 2). Among the key parameters are whether GNP volume fraction, pattern and distribution, laying sequences, and geometric dimension, etc., have effects on the mechanical behaviors of this type of composites. Unless otherwise specified, all the plate specimens have the same thickness in the cross-sectional direction and are set with simply supported boundary conditions. Fixed at length to width ratio (*b*/*a*): 1.0. 0/90/0/90/0 symmetric balanced layup structure is used here. The physical characteristics of the resin medium and the GNP fillers are specified below: $E_{MAT} = 2.5\text{GPa}$, $\nu_{MAT} = 0.34$, $E_{11}^{GNP} = 1812\text{GPa}$, $E_{22}^{GNP} = 1807\text{GPa}$, $G_{12}^{GNP} = 683\text{GPa}$, $\nu_{12}^{GNP} = 0.177$, $\alpha_{11}^{GNP} = -0.90 \times 10^{-6}K^{-1}$, $\alpha_{22}^{GNP} = -0.95 \times 10^{-6}K^{-1}$, $\alpha_{MAT} = 45 \times 10^{-6}K^{-1}$, $\beta_{11}^{GNP} = 0.00026(wt\%H_2O)^{-1}$, $\beta_{22}^{GNP} 0.00027(wt\%H_2O)^{-1}$, β_{MAT} $0.00268(wt\%H_2O)^{-1}$. Table 1 displays the efficiency parameters associated with various GNP content proportions [58]. Displacements and stresses are normalized by: $(\overline{u}, \overline{w}) = (u, 100w)/\alpha_{MAT}aT_i$, $(\overline{\sigma}_x, \overline{\sigma}_y, \overline{\tau}_{xy}, \overline{\tau}_{xz}) = (\sigma_x, \sigma_y, \tau_{xy}, \tau_{xz})/E_{MAT}\alpha_{MAT}T_i$, i=0,1,2. This research section investigates the hygrothermal performance of FG-GNPRC panels subjected to integrated thermal and humidity loads (T_0=100, C_0=0.001). The computational data presented in Table 2 demonstrate that variations in the graphene nanoplatelet volume ratio significantly affect the lateral deflection, and such an effect remains consistent across various span-to-thickness proportions (*a/h*). It is observed that when the GNP content increases by only 2%, the corresponding transverse displacement rises by about 58%, indicating a strong sensitivity of the structural response to GNP addition. The large increase is caused by the difference in thermal and moisture expansion between graphene nanoplatelets and the polymer matrix. This difference increases internal constraint and causes strong strain mismatch through the thickness under temperature and moisture loads. This behavior can be associated with the modification of the effective hygrothermal expansion properties of the polymer composite after introducing graphene nanoplatelets. In addition, the deflection response is affected by the plate thickness. As the thickness increases, the contribution of GNP reinforcement becomes more evident, which may be related to stronger interfacial interactions between the nanoplatelets and the matrix material through the thickness direction. These results suggest that the effectiveness of GNP reinforcement under hygrothermal loading is strongly affected by the plate dimensions. The numerical analysis therefore confirms that incorporating GNPs can influence both the hygrothermal deformation characteristics and the stiffness performance of FG-GNPRC plates. According to the analysis of Fig. 13, investigate the stress distribution conditions of the four different types of FG-GNPRC plates under the hygrothermal loading (T_0=T_1=100, C_0=C_1=0.001). The results show that the stress maps show evident divergence features, and the stress-strain curves vary more profoundly under the influence of graphene nanoplatelet gradient distribution attributes. With respect to in - plane stress components there exists a direct positive relationship amongst the volume fraction of GNPs and the magnitude of the hygrothermal stress. The FG-X distribution configuration shows the highest stress in both surface layers, which is attributed to the stepped concentration gradient that enhances the impact of hygrothermal gradient. The stepped concentration gradient creates stiffness differences between adjacent layers. These stiffness differences increase interfacial shear transfer and raise local stress under hygrothermal expansion. In addition, transverse shear stress also exhibits a similar dependence on the volume fraction of GNP, but the distribution pattern is different. By comparison, there is a large amount of stress concentration in the two innermost layers of the FG-O configuration. These results prove that the planned arrangement of GNP distribution can be used to regulate the hygrothermal properties of FG-GNPRC structures. By adjusting the spatial distribution of nanoparticles, it is now possible to design stress conditions that enhance key areas of strength or weaken weak interface locations by optimizing structure.

An investigation on the stress distribution characteristics of FG-GNPRC plates based on their lamination schemes: compare LS-1 $(0/90/0/90/0)_s$, LS-2 $(0/90)_s$, and LS-3 $(90/0/90/0/90)_s$; supplement to FGM-O allocation layout as Figs. 14-15, which shows that there will be a considerable effect from layer arrangement order on its stress distributions. Accordingly, at some stage in the process, it may have some extentable effect on the stress during lamination order reaches a certain threshold; Moreover, an optimised stacking order can also modify its corresponding responses. Because there is a certain degree of interaction between these directions, as well as anisotropy characteristics at each plie point, leading to such alterations. The change in ply direction affects the directional stiffness, Thermal expansion or moisture expansion for a laminated part. This leads to an unbalanced stiffness and strain distribution because of different thicknesses, thus changing the interlayer stress field through shear transfer mechanisms. These factors' integrated results ultimately determine the final stress distribution pattern; therefore, in future research on

10.57647/jnsc.2026.1605.23

laminated structures for specific purposes, we must achieve desirable structural properties using FG-GNPRC systems. Thereafter, the study for effects of hygrothermal conditions on bending deformation for FG-GNPRC panels will be carried out next. Fig. 16 shows the deformation and stress of FG-GNPRC plate (FG-X Layout) under different humidity-temperature combinations. Based on a significant impact of the effects of hydrothermal loads on planar displacement fields and stress shape distributions, as well as load-dependent thickness-through distributions that regulate plates' two-directional deformation forms and stress conditions.

Additionally, T_0=T_1=100, C_0=C_1=0.001 can produce the greatest inter-laminate shear force. A large amount of regular deformation appears due to both temperature and moisture differences together at this height. The difference causes greater interface shear stress under expansion restraint constraints.

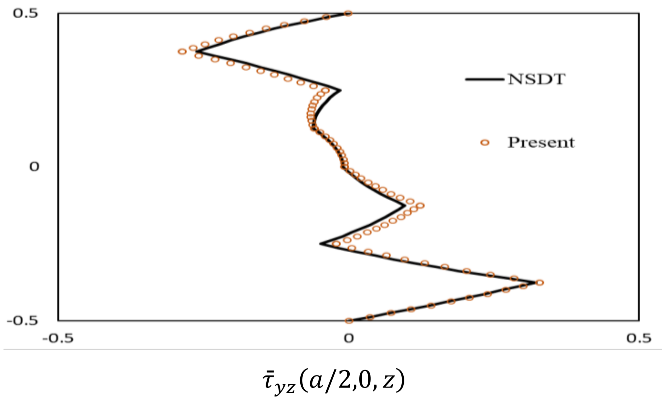

Figure 12. Transverse shear stress variations in the 8-layer composite plate (*a/h*=5)

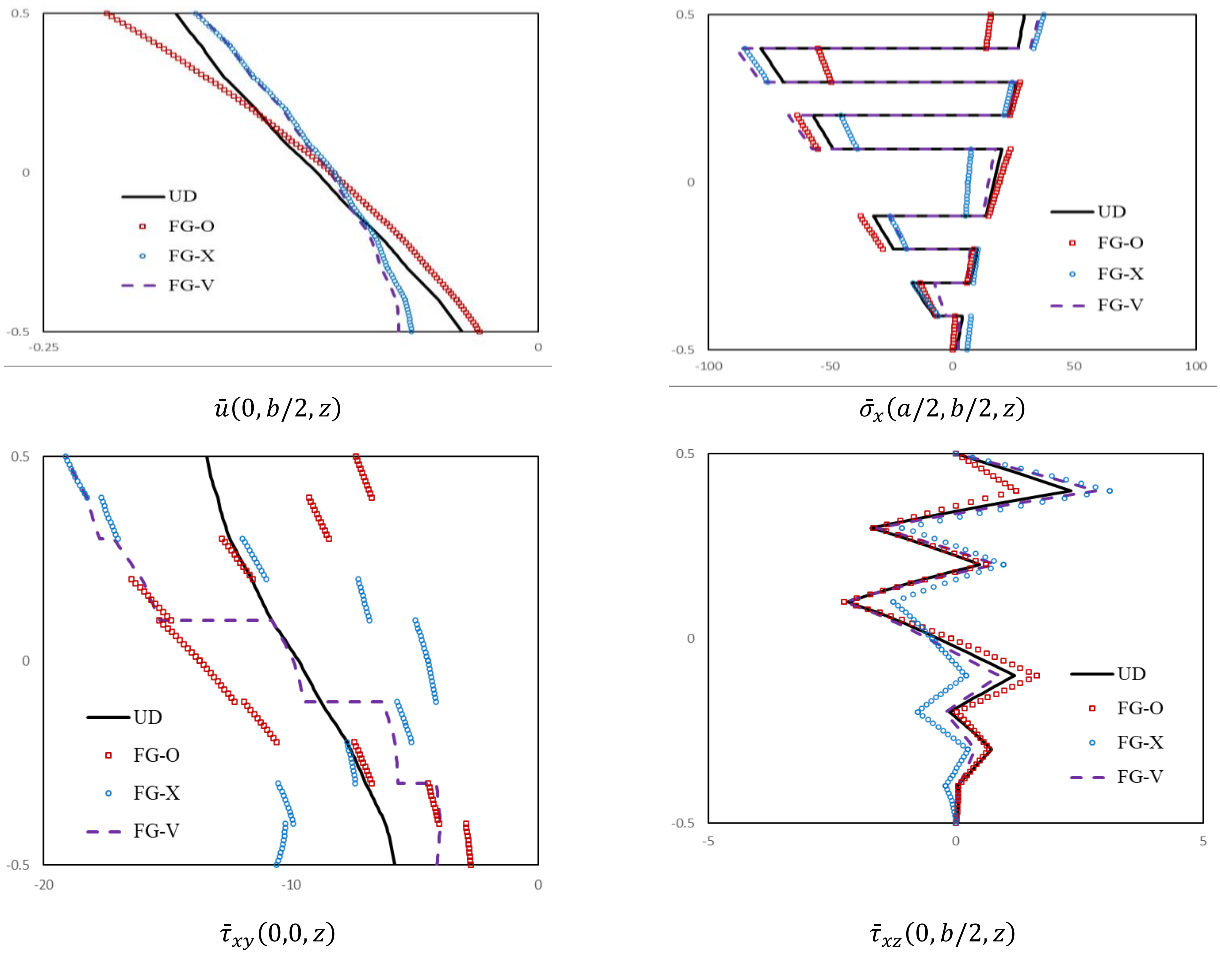

Figure 13. Displacement and stress results of the FG-GNPRC plate for different graphene distribution types (T_0= T_1=100, C_0= C_1=0.001, *a/h*=5)

10.57647/jnsc.2026.1605.23

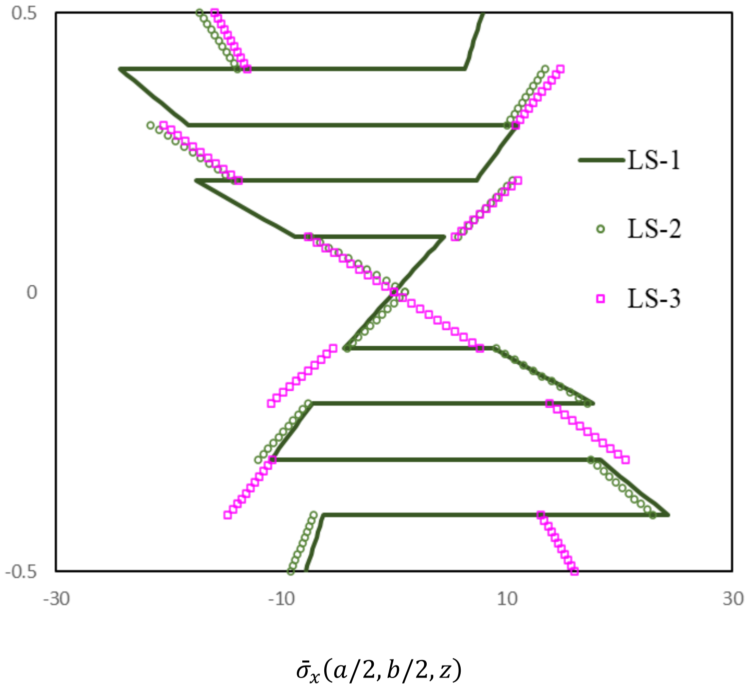

Figure 14. In-plane stress variations of the FG-GNPRC plate subjected to hygrothermal loading (T_1=100, C_1=0.001, a/h=5)

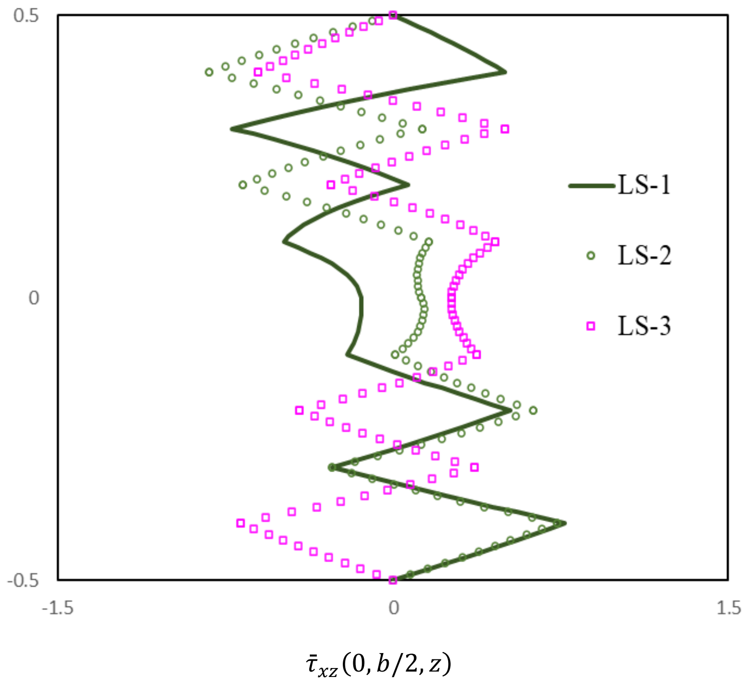

Figure 15. Transverse shear stress variations of the FG-GNPRC plate subjected to hygrothermal loading (T_1=100, C_1=0.001, a/h=5)

Table 1. Graphene enhancement factors across volume fractions

V_G	δ_1	δ_2	δ_3
0.03	2.929	2.855	11.842
0.05	3.068	2.962	15.944
0.07	3.013	2.966	23.575
0.09	2.647	2.609	32.816
0.11	2.311	2.260	33.125

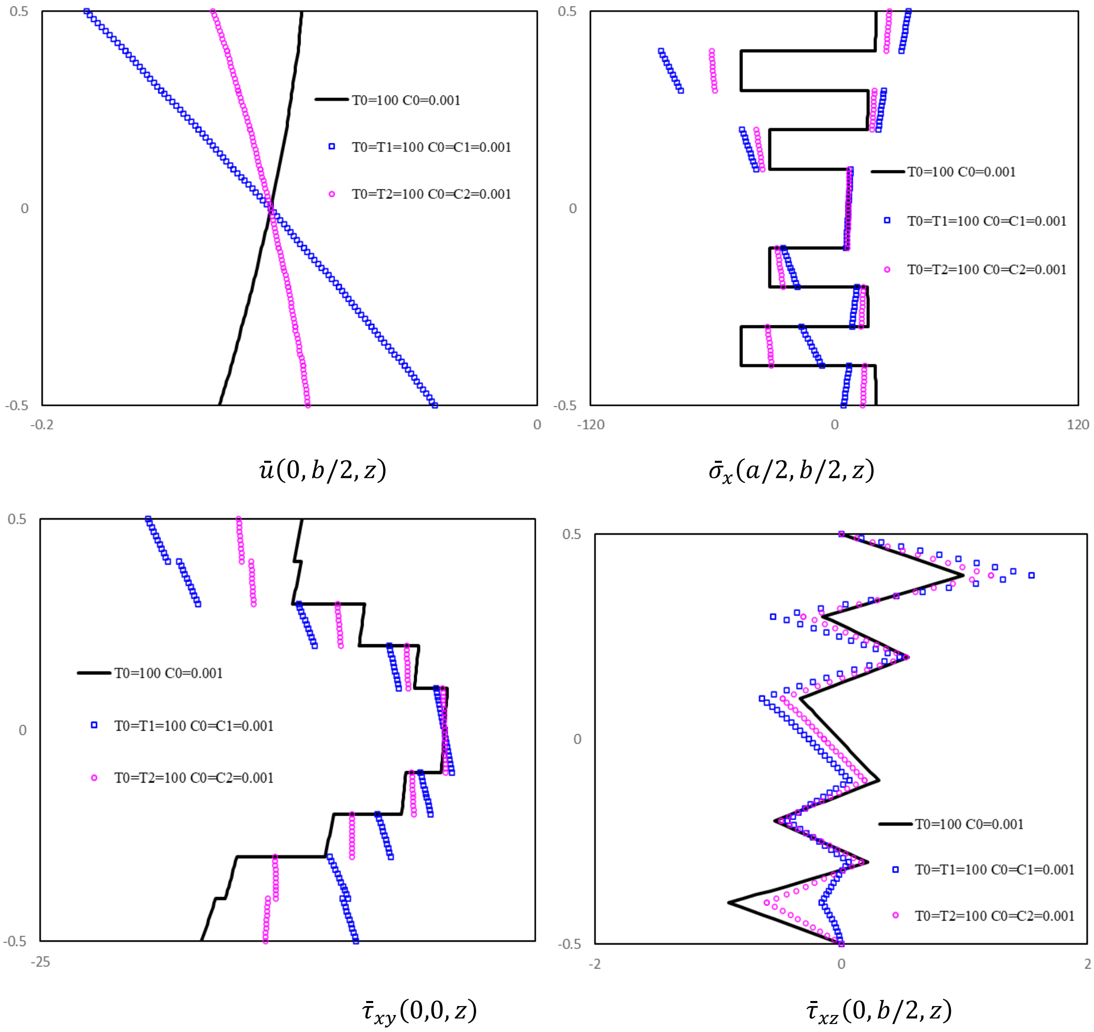

Figure 16. Displacement and stress results of the FG-GNPRC plate under various hygrothermal loads (*a/h*=10

Table 2. Transverse displacements of UD FG-GNPRC plates for various span-to-thickness ratios ($\bar{w}(a/2, b/2, h/2)$, T_0=100, C_0= 0.001)

Volume fraction V_G	*a/h*				
	5	10	20	50	100
0.03	0.1987	0.0997	0.0503	0.0210	0.0116
0.05	0.4724	0.2365	0.1187	0.0483	0.0253
0.07	0.7461	0.3734	0.1871	0.0756	0.0389
0.09	1.0198	0.5102	0.2555	0.1029	0.0525
0.11	1.2935	0.6470	0.3239	0.1302	0.0661

Table 3. Displacement and stresses of FG-GNPRC plates (FG-X configuration) under diverse hygrothermal loads

Hygrothermal Loads	$\bar{u}\left(0, \frac{b}{2}, \frac{h}{2}\right)$	$\bar{\sigma}_x\left(\frac{a}{2}, \frac{b}{2}, \frac{h}{2}\right)$	$\bar{\tau}_{xy}\left(0, 0, \frac{h}{2}\right)$	$\bar{\tau}_{xz}\left(0, \frac{b}{2}, \frac{2h}{5}\right)$
T_0=100, C_0=0.001	-0.0952	20.621	-11.773	0.9911
T_0= T_1=100,	-0.1822	36.596	-19.546	1.5431
C_0= C_1=0.001	(91.4%)	(77.5%)	(66.0%)	(55.7%)
T_0= T_2=100,	-0.1310	27.153	-14.974	1.2171
C_0= C_2=0.001	(37.6%)	(31.7%)	(27.2%)	(22.8%)

10.57647/jnsc.2026.1605.23

Table 4. Displacement and stresses of FG-GNPRC plates (FG-O configuration) under hygrothermal load (T_0= T_1=100, C_0= C_1=0.001, a/h=10)

GNP Size	$\bar{w}\left(\frac{a}{2},\frac{b}{2},\frac{h}{2}\right)$	$\bar{\sigma}_x\left(\frac{a}{2},\frac{b}{2},\frac{h}{2}\right)$	$\bar{\tau}_{xy}\left(0,0,\frac{h}{2}\right)$	$\bar{\tau}_{xz}\left(0,\frac{b}{2},\frac{2h}{5}\right)$
a_G/t_G=100, b_G/t_G=100	58.711	19.611	-7.7234	1.4125
a_G/t_G=500, b_G/t_G=100	62.613	28.175	-8.6386	1.7285
a_G/t_G=1000, b_G/t_G=100	63.828	31.379	-8.9498	1.8622
a_G/t_G=100, b_G/t_G=500	65.764	40.564	-9.3185	2.9124
a_G/t_G=100, b_G/t_G=1000	67.362	48.206	-9.7324	3.4638

Table 3 also presents deformed structures and stress states of the FG-GNPRC with an FG-X configuration under different hygrothermal load conditions. The first row (T_0=100, C_0=0.001) is taken as a reference case. There is a clear trend that shows the combination method has an effect on increasing displacement, stress respectively than the original one when using single-hydrothermal load.

The values in brackets are expressed as the percentage rise compared with those of the base case. In terms of the humid-load case (T_0=T_1=100, C_0=C_1=0.001), The values for all parameters were very large and showed a large percentage change, which ranged from 55.7% to 91.4%. Thus, adding either a combined uniform or linear-hygrothermal-load functional form enhances the mechanical effect at some level. Under the combined influence of a uniform load and a sine wave loading, the change in water level was also minor, falling within an acceptable range from 22.8%~37.6%. It shows that the existence of a hygrothermal field significantly affects the structural response of the FG-GNPRC plate. Given that gradient conditions (T_0=T_2=100, C_0=C_2=0.001) have produced a milder mechanical response than those of type T_0=T_1=100, C_0=C_1=0.001. As shown in Table 4, under the conditions that the temperature and humidity were at T_0=T_1=100, C_0=C_1=0.001 for the FG-O layout FG-GNPRC plate subjected to hygrothermal action. Research on the effects of dimension factors for GNP particles on the structures of FG-GNPRC plate. Different results on different paths. When b_G/t_G is fixed at 100 and a_G/t_G changes from 100 to 1000, there will be an approximately equal amount added. The first parameter has increased from 58.711 to 63.828; The absolute value of the third (neglectable) term has risen from 7.7234 to 8.9498. Increasing the length-to-diameter ratio (a/h) of GNPs can improve both stiffness and load-bearing capacity in FG-GNPRC plate under specified hygrothermal condition. The more pronounced the effect depends on the condition of the b_G/t_G ratio when maintaining a_G/t_G=100. From 100 to 1000, as b_G/t_G increases, the value will increase significantly. The first parameter went up from 58.711 to 67.362; the second one went sky-high from 19.611 to 48.206. It can be seen from this that, in terms of the influence of width-thickness ratio on mechanical properties due to its effect on the effective load transmission path and reinforcing structure configuration within the polymer matrix. The geometry of the reinforcing GNPs serves as an important design parameter in these results. The large-aspect-ratio of the wide direction in width (b_G/t_G) significantly affects the displacements and stress fields under humidification-stabilization loads applied to an FG-GNPRC plate structure. Therefore, it is also more significant for its mechanical performance index.

4.3. Conclusions

In this study, a novel hygrothermal model including the effect of transverse normal strain is developed for FG-GNPRC plates. Based on the hygrothermal-induced transverse normal deformation but no need to add displacement variables, present model can keep high efficiency of computation, overcome inherent defects of traditional methods in solving hygrothermal problem. Findings and Conclusions summary are the main form are following: This study shows that the presented model yields accurate predictions for the displacement and stress states in FG-GNPRC plates subjected to hygrothermal loading. Although the conventional higher-order theories ignoring the effect of transverse normal strain have significant errors in predicting the hygrothermal stress field. This result is our imitation to have the transverse normal deformation of the composite model with high fidelity to hygrothermal behavior. Graphene nanoplatelets add as even small quantities increase hygrothermal expansion coefficients, increasing transverse deformation of FG-GNPRC plates. But it is clear from the data is that it is because of the enhancement caused by graphene nanoplatelets will gradually decline when the volume fraction is gradually increased. Spatial distribution and gradation of GNP are ways of controlling the stress development in FG-GNPRC plates. The gradation of increase in GNP concentration in some layers will lead to an increase in the level of hygrothermal stress resulting from the different expansion coefficients in different layers. More parametric study shows that hygrothermal load, Geometric size and Stacking Sequence decide the deformation characteristic and stress condition of such composite system. The results will be guidance to us that how the stress would change in the combined temperature and humidity action on the FG-GNPRC plates. Also, the theory to make systematic Design methods for taking the advantage of multi-functionalities of GNP reinforcements is prepared by this study. To modify the material structure, optimize interface engineering to enhance the hygrothermal stability of composite structures under harsh working conditions.

Acknowledgement

The work described in this paper was supported by the Joint Fund of Zhejiang Provincial Natural Science Foundation of China [No. LQZQN25E020002]; the National Natural Science Foundation of China [No. 12302196]; the Quzhou Science and Technology Bureau Project [2025K191]. Central Government-Guided Local Science and Technology Development Fund Project: Construction of Zhejiang Key Laboratory of Intelligent Manufacturing for Aerodynamic Equipment (No. 2025ZY01027). Zhejiang Key Laboratory of Intelligent Manufacturing for Aerodynamic Equipment (No. 2025E10033).

Authors' Contributions

All authors contributed to the conception and design of the study.
Conceptualization: Rui Ma, Manyu Zhang and Qilin Jin.
Methodology: Rui Ma, Sadam Hussain, and Abdul Ghaffar.
Formal analysis: Rui Ma, Yuan Hu, and Mingran Zhang.
Investigation: Rui Ma, Abdul Ghaffar and Hongliang Li.
Validation: Fanzeng Guo and Yuan Hu.
Funding acquisition: Rui Ma, and Qilin Jin.
Writing—original draft: Rui Ma, Manyu Zhang and Qilin Jin.
Writing—review & editing: Rui Ma, Manyu Zhang, Qilin Jin, and Hongliang Li.
Supervision: Manyu Zhang and Qilin Jin.

Availability of data and materials

The data supporting the findings of this study are available within the article. Additional data related to this work are available from the corresponding author upon reasonable request.

Conflicting Interests

The author(s) declared no potential conflicts of interest with respect to the research, authorship, and/or publication of this article.

References

[1] Ma GS, Chen YB, Xia L, Zhan YF, Zhong B, Yang H, Huang LN, Xiong L, Huang XX, Wen GG. Mechanical and thermal properties of Graphene nanoplates (GNPs)/Lithium aluminosilicate (LAS) composites: an analysis based on mathematical model and experiments. *Ceram Int*. **46**, 10903-10909(2020)

[2] Zhang HM, Zhang GC, Tang M, Zhou LS, Li HW, Fan X, Shi XT, Qin JB. Synergistic effect of carbon nanotube and graphene nanoplates on the mechanical, electrical and electromagnetic interference shielding properties of polymer composites and polymer composite foams. *Chem Eng J*. **353**, 381-393(2018)

[3] Hoang VNV, Thanh PT. A new trigonometric shear deformation theory for free vibration of graphene reinforced metal-matrix nanocomposite plate submerged in fluid medium. *Thin-Walled Struct*. **184**, 110472(2023)

[4] Yee K, Khaniki HB, Ghayesh MH, Ng CT. Free vibrations of cracked functionally graded graphene platelets reinforced Timoshenko beams based on Hu-Washizu-Barr variational method. *Eng Struct*. **293**, 116587(2023)

[5] Ding HX, Eltaher MA, She HL. Nonlinear low-velocity impact of graphene platelets reinforced metal foams cylindrical shell: effect of spinning motion and initial geometric imperfections. *Aerosp Sci Technol*. **140**, 108435(2023)

[6] Arefi M, Tabatabaeian A, Mohammadi M. Bending and stress analysis of polymeric composite plates reinforced with functionally graded graphene platelets based on sinusoidal shear-deformation plate theory. *Def Technol*. **17**, 64-74(2021)

[7] Yang N, Zou Y, Arefi M. Bending results of graphene origami reinforced doubly curved shell. *Def Technol*. **35**, 198-210(2024)

[8] Shen H, Xiang Y, Fan Y. Postbuckling of functionally graded graphene-reinforced composite laminated cylindrical panels under axial compression in thermal environments. *Int J Mech Sci*. **135**, 398-409(2018)

[9] Ebrahimi F, Hafezi P, Dabbagh A. Buckling analysis of embedded graphene oxide powder-reinforced nanocomposite shells. *Def Technol*. **17**, 226-233(2021)

[10] Sahmani S, Kotrasova K, Zareichian M, Sun J, Babak Safaei. Nonlinear asymmetric thermomechanical buckling of shallow nanoscale arches having dissimilar end conditions embracing nonlocality and strain gradient size dependencies. *Def Technol*. **47**, 67-82(2025)

[11] Lv Y, Zhang J, Wu JY, Li LH. Mechanical and thermal postbuckling of functionally graded graphene origami-enabled auxetic metamaterials plates. *Eng Struct*. **298**, 117043(2024)

[12] Hoang VNV, Shi P, Toledo L, Vu H. Thermal vibration analysis of FG-GPLRC doubly curved shells partially resting on Kerr foundation based on higher-order shear deformation theory. *Thin-Walled Struct*. **195**, 111357(2024)

[13] Eyvazian A, Zhang CW, Alkhedher M, Muhsen S, Elkotb MA. Thermal buckling and post-buckling analyses of rotating Timoshenko microbeams reinforced with graphene platelet. *Compos Struct*. **304**, 116358(2023)

[14] Bidzard A, Malekzadeh P, Mohebpour SR. A size-dependent nonlinear finite element free vibration analysis of multilayer FG-GPLRC toroidal micropanels in thermal environment. *Compos Struct*. **279**, 114783(2022)

[15] Khorasani M, Soleimani-Javid Z, Arshid E. Thermo-elastic buckling of honeycomb micro plates integrated with FG-GNPs reinforced Epoxy skins with stretching effect. *Compos Struct*.

258, 113430(2021)

[16] Sobhy M. Differential quadrature method for magneto-hygrothermal bending of functionally graded graphene/Al sandwich-curved beams with honeycomb core via a new higher-order theory. *J Sand Struct Mater*. **23**, 1662-1700(2021)

[17] Mojiri HR, Salami SJ. Free vibration and dynamic transient response of functionally graded composite beams reinforced with graphene nanoplatelets (GPLs) resting on elastic foundation in thermal environment. *Mech Based Des Struct Mach*. **50**, 1872-1892(2022)

[18] Eroğlu M, Koç MA, Esen İ. Thermomechanical free vibration buckling of FG graphene-reinforced doubly-curved sandwich shells. *Adv Eng Software*. **202**, 103875(2025)

[19] Zhang Y, Guo XK, Ni Z, Zhang YY, Zhang H, Lü CF, Yang J. Nonlinear frequency analysis of piezoelectric functionally graded porous plates reinforced by graphene platelets under thermo-electro-mechanical loads. *Mech Adv Mater Struct*. **33**, 2456686(2026)

[20] Nam VH, Tu BT, Hung VT, Doan CV, Phượng NT. Nonlinear thermomechanical buckling and postbuckling analysis of sandwich FG-GPLRC complexly curved caps and circular plates with porous core. *Acta Mech*. **236**, 421-438(2025)

[21] Li L, Shi ZW, Peng W, He TH. Thermoelastic bending wave propagation of FG hybrid nanocomposite microbeam reinforced by GPLs and CNTs under fractional order nonlocal elasticity theory. *J Therm Stress*. **47**, 1500-1518(2024)

[22] Bui TT, Vu MD, Pham NN. Nonlinear thermo-mechanical dynamic buckling and vibration of FG-GPLRC circular plates and shallow spherical shells resting on the nonlinear viscoelastic foundation. *Arch Appl Mech*. **94**, 3715-3729(2024)

[23] Liu T, Sun XR, Hu WF, Wang L, Zhang SQ, Bui TQ. Nonlinear thermal-mechanical coupled isogeometric analysis for GPLs reinforced functionally graded porous plates. *Eng Struct*. **319**, 118827(2024)

[24] Li ZC, Hu D, Shen ML, Huang H, Ou ZH. Thermal upheaval buckling framework of a graphene-reinforced subsea pipeline laid on an arched concave seabed. *Eng Struct*. **318**, 118750(2024)

[25] Li M, Lu L, She GL. Thermal post-buckling analysis of functionally graded graphene platelets reinforced composite microtubes. *Thin-Walled Struct*. **203**, 112246(2024)

[26] Nam VH, Ly LN, My DTK, Duc VM, Phượng NT. On the nonlinear buckling and postbuckling responses of sandwich FG-GRC toroidal shell segments with corrugated core under axial tension and compression in the thermal environment. *Polym Composite*. **45**, 13737-13752(2024)

[27] Songsuwan W, Thai S, Wattanasakulpong N. Buckling and post-buckling behavior of ideal and non-ideal FG-GPLRC beams in thermal environment. *Acta Mech Sin*. **41**, 424374(2025)

[28] Ying YF, Zhao LC, Kumar A. Higher-order buckling analysis of FG porous cylindrical micro-shells integrated with GPLs-RC patches in hygrothermal environment immersed on Kerr foundation. *Acta Mech*. **235**, 1785-1802(2024)

[29] Ahmadi O, Rash-Ahmadi S. Geometrically nonlinear post-buckling of advanced porous nanocomposite lying on elastic foundation in hygrothermal environment. *Acta Mech*. **234**, 2725-2743(2023)

[30] Sobhy M. Differential quadrature method for magneto-hygrothermal bending of functionally graded graphene/Al sandwich-curved beams with honeycomb core via a new higher-order theory. *J Sand Struct Mater*. **23**, 1662-1700(2021)

[31] Zhao J, Gao ZJ, Li H, Guan JL, Han QK, Wang QS. A unified modeling method for dynamic analysis of CFRC-PGPC circular arche with general boundary conditions in hygrothermal environment. *Compos Struct*. **255**, 112884(2021)

[32] Zhao J, Hu JZ, Wang TH, Li H, Guan JL, Liu JC, Gao ZJ. A unified modeling method for dynamic analysis of GPLs-FGP sandwich shallow shell embedded SMA wires with general boundary conditions under hygrothermal loading. *Eng Struct*. **250**, 113439(2022)

[33] Oun A, Alajarmeh O, Manalo A, Abousnina R, Gerdes A. Durability of hybrid flax fibre-reinforced epoxy composites with graphene in hygrothermal environment. *Constr Build Mater*. **420**, 135584(2024)

[34] Mishra K, Singh A. Effect of graphene nano-platelets coating on carbon fibers on the hygrothermal ageing driven degradation of carbon-fiber epoxy laminates. *Compos Part B-Eng*. **269**, 111106(2024)

[35] Cheng YH, She GL. Nonlinear dynamics of rotating graphene-reinforced composite blades under 1:2 internal resonance in fluid-submerged environments. *Ocean Enge*. **341**, 122717 (2025)

[36] Zhao B, She GL. Vibration analysis of graphene reinforced metal foam coupled plates under arbitrary boundary and coupled conditions. *Eng Structs.* **343**, 121143 (2025)

[37] Zhao B, Eltaher MA, She GL. Dynamic response analysis of acoustic black hole plates with cutouts under arbitrary boundary constraints. *Thin-Walled Struct*. **217**, 113859 (2025)

[38] Zhang ZP, Wang YW, Zhang W. Temperature- and moisture-dependent aeroelastic stability of graphene platelet reinforced nanocomposite lattice sandwich plates subjected to supersonic flow. *Aerosp Sci Technol*. **138**, 108348(2023)

[39] Zhang CW, Jin Q, Song YS. Vibration analysis of a sandwich cylindrical shell in hygrothermal environment. *Nanotechnol Rev*. **10,** 414-430(2021)

[40] Yao MH, Wang SC, Niu Y, Wu QL, Wang C. Vibration characteristics of pre-twisted rotating Ti-SiC composite airfoil blade. *Appl Math Model*. **128**, 392-409(2024)

[41] Niu Y, Zhang W, Guo XY. Free vibration of rotating pretwisted functionally graded composite cylindrical panel reinforced with graphene platelets. *Euro J Mech A-Solids*. **77**, 103798(2019)

[42] An HL, Yang SW, Wan YG, Niu Y. Study on natural vibration characteristics of FG-GPLRC cantilever trapezoidal plates with perovskite surface layer. *In J Struct Stab Dyn*. (2026)

[43] Wang ZQ, Yang SW, Hao YX, Zhang WL, Wensai Ma, Niu Y. High-dimensional nonlinear flutter suppression of variable thickness porous sandwich conical shells based on nonlinear energy sink. *J Sound Vib*. **595**, 118731(2025)

[44] Wan YG, Yang SW, An R, Wang ZQ, Yang HL. Free vibration of hinged FG-GPLRC magneto-electro-elastic variable-thickness folded trapezoidal sandwich panels. Acta Mech Sinica-PRC. **42**, 525120(2026)

[45] Carrera E. Cz0 requirements-models for the two dimensional analysis of multilayered structures. *Compos Struct*. **37**, 3-4(1997).

[46] Sharifi M, Marjani A, Mahdavian L, Shamlouei HS. Density

functional theory study of dyes removal from colored wastewater by a nano-composite of polysulfone/polyethylene glycol. *J Nanostructure Chem*. **13**, 519-532(2022)

[47] Sohrabi B, Karimi A, Chenab KK. The ZnS–CuS thin layer nanocomposites green synthesis and their efficient photocatalytic applications in photodegradation the organic dye molecules. *J Nanostructure Chem*. **13**, 533-543(2023)

[48] Panchami HR, Isloor AM, Ismail AF. Improved hydrophilic and antifouling performance of nanocomposite ultrafiltration zwitterionic polyphenylsulfone membrane for protein rejection applications. *J Nanostructure Chem*. **12**, 22(2022)

[49] Jin QL, Yao WA. Hygrothermal analysis of laminated composite plates in terms of an improved C^0 -type global local model. *Aerosp Sci Technol*. **63**, 328-343(2017).

[50] Wu Z, Ren XH. Finite element analysis of hygrothermal effects on angle-ply composite plates. *J Compos Mater*. **50**, 2215-2233(2016)

[51] Wu Z, Lo SH. Hygrothermomechanical effects on laminated composite plates in terms of a higher-order global-local model. *J Therm Stresses*. **38**, 543-568(2016).

[52] Cho M, Oh J. Higher order zig-zag theory for fully coupled thermo-electric-mechanical smart composite plates. *Int J Solids Struct*. **41**,1331-1356(2004)

[53] Bhaskar K, Vardan TK, Ali JSM. Thermo-elastic solution for orthotropic and anisotropic composite laminates. *Compos Part B-Eng*. **27**, 415-420(1996)

[54] Murakami H. Laminated composite plate theory with improved in-plane response. *J Appl Mech*. **53**, 661-666(1986)

[55] Reissner E. On a certain mixed variational theorem and a proposed application. *Int J Numer Methods Eng*. **20**, 1366-1368(1984)

[56] Matsunaga H. A comparison between 2-D single-layer and 3-D layerwise theories for computing interlaminar stresses of laminated composite and sandwich plates subjected to thermal loadings. *Compos Struct*. **64**,161-177(2004)

[57] Reddy JN. A simple higher-order theory for laminated composite plates. *J Appl Mech*. **51**,745-752(1984)

[58] Shen HS, Xiang Y, Lin F. Nonlinear vibration of functionally graded graphene-reinforced composite laminated plates in thermal environments. *Comput Method Appl Mech Eng*. **319**,175-193(2017)